DEVELOPMENT OF SMALL-SCALE THERMOACOUSTIC ENGINE AND THERMOACOUSTIC COOLING DEMONSTRATOR

By

NAJMEDDIN SHAFIEI-TEHRANY

Masters in Mechanical Engineering

Washington State University
School of Mechanical and Material Engineering

May 2008

To the Faculty of Washington State University

The members of the Committee appointed to examine the thesis of Najmeddin Shafiei-Tehrany find it satisfactory and recommend that it be accepted.

_____
Chair

_____

_____

Acknowledgements

Many special thanks go to my advisor, Dr. Konstantin Matveev, for the guidance he gave me during my graduate studies. Without his help and patience I would not have succeeded. I also extend my gratitude to Mr. John Rutherford, machinist at The Science Shop, and Mr. Kurt Hutchinson, machinist at The Mechanical and Materials Engineering Shop, for their professionalism and the time they spent on manufacturing the components of the thermoacoustic engine and the refrigeration system. I am also grateful for the assistance provided by Mr. Robert Lentz during the entire research. I also would like to thank the Mechanical Shop for allowing me to use their machines to manufacture necessary parts at my convenience. I also would like to thank Dr. Mike Anderson for all the help and support he showed throughout my research. Finally I would like to thank my committee, Prof. Robert Richards and Prof. Cecilia Richards, for honoring me with their participation.

Development of Small-Scale Thermoacoustic Engine and Thermoacoustic Cooling Demonstrator

Abstract

By Najmeddin Shafiei-Tehrany, M.S.
Washington State University
May 2008

Chair: Konstantin Matveev

Thermoacoustics is a science and technology field that studies heat and sound interactions. Sound waves in any fluid consist of coupled pressure, motion, and temperature oscillations. When the sound travels through a narrow channel, an oscillating heat flow between the fluid and the channel's wall becomes significant. The present study deals with the effects of thermoacoustic cooling with closed and open ended tubes and also investigates the performance of a small-scale thermoacoustic heat engine.

The first part of this document presents the design, construction, and testing of a miniature standing-wave thermoacoustic heat engine. The main objective was to build and test a miniature heat engine without moving parts. Recorded parameters included the temperature difference across the stack and the corresponding acoustic pressure amplitude of the sound produced by the engine. The system was also tested for different stack materials and tube lengths. The most efficient system is described in detail in this document. The critical temperature difference across the stack was measured to be approximately 350°C for the 5.8 cm engine and 250°C for the 9.3 cm engine. The average acoustic RMS pressure of the sound produced was about 2.7 Pa at 30 cm from the engine for both lengths and the frequency of the sound was about 1.4 kHz for the 5.8 cm engine and about 1 kHz for the 9.3 cm engine.

The second part of this document presents the effects of thermoacoustic cooling with closed and open ended tubes. The position of the stack and sound frequencies were varied to

establish the most effective configuration. For each configuration, the pressure amplitude inside the tube and the sound frequency were the controlled parameters, and the temperature difference across the stack was measured. The experimental results of the thermoacoustic cooling system are compared to the theoretical results. For the closed-end system the temperature of the top of the stack was higher than the bottom and for the open-end system the temperature of the top of the stack was lower than the bottom. The maximum temperature difference was about 32°C for the closed-end and 16°C for the open-end.

TABLE OF CONTENTS

Acknowledgements iii

Abstract iv

List of Symbols vii

List of Tables ix

List of Figures x

1. Introduction 1

1.1. Background 2
1.1.1. Heat Engine 4
1.1.2. Refrigerator 5

1.2. Objectives 6

2. Methodology 8

2.1. Theoretical Formulation 9
2.1.1. Heat Engine 9
2.1.2. Refrigerator 19

2.2. Experimental Setups 23
2.2.1. Heat Engine 23
2.2.2. Refrigerator 25

3. Results and Discussions 30

3.1. Heat Engine 31

3.2. Cooling Demonstrator 43
3.2.1. Closed-End System 43
3.2.2. Open-End System 52

4. Conclusions and Recommendations 60

5. Bibliography 64

List of Symbols

a	speed of sound
c_p	isobaric heat capacity per unit mass
D	diameter of the stack
D_{hx}	diameter of the heat exchanger
h	spacing between the stack plates
h_{hx}	spacing between the heat exchanger plates
k	fluid thermal diffusivity
K	fluid thermal conductivity
K_S	solid thermal conductivity
l	stack's plate half-thickness
l_{hx}	heat exchanger's plate half-thickness
L	resonator length
p^s	acoustic pressure waveform
P_A	acoustic pressure amplitude
R	radius of the resonator
R_g	air gas constant
T_m	mean temperature
∇T_m	mean temperature gradient across the stack
∇T_{crit}	ideal critical temperature gradient across the stack
ΔT	temperature difference across the stack
u^s	acoustic velocity waveform
x	coordinate along the resonator
x_S	stack position
Δx	stack length
Δx_{hx}	heat exchanger length
y_0	half-spacing between plates of the stack
y_{0hx}	half-spacing between plates of the heat exchanger
γ	ratio of specific heats
ε_s	stack's plate heat capacity ratio
σ	Prandtl number
Γ	normalized temperature gradient
Π	cross-sectional perimeter of the stack surface
Π_{hx}	cross-sectional perimeter of the heat exchanger surface
ω	angular frequency
λ_{rad}	radian wavelength

λ	acoustic wavelength
β	thermal expansion coefficient
ρ_m	mean density
ν	kinetic viscosity
μ	dynamic viscosity
δ_k	thermal penetration depth of the fluid
δ_s	thermal penetration depth of the solid material
δ_ν	viscous penetration depth of the fluid

List of Tables

1. Tabulated Temperature Uncertainty Calculations 33

2. Tabulated Temperature Uncertainty Calculations 33

3. Tabulated Results of the Acoustic Pressure RVC 100 PPI 39

4. Tabulated Results of the Acoustic Pressure for RVC 80 PPI 40

5. Tabulated Results of the Acoustic Pressure for Steel Wool 40

6. Pressure Uncertainty Calculations for 5.8 cm Engine at Different Angles 41

7. Tabulated experimental and theoretical results for both 5.8 and 9.3 cm engines 42

8. Uncertainty Calculations for Different RMS Pressures 49

9. Uncertainty Calculations for Different Stack Positions 49

10. Uncertainty Calculations for Different Stack Positions 57

11. Uncertainty Calculations for Different RMS Pressures 58

List of Tables

1. Two Types of Heat Engine 3

2. (a) Schematic of Thermoacoustic Engine 9
   (b) Expanded View of the Stack Plates 9
   (c) Pressure and Velocity Waveforms along the Resonator 9

3. Locations of Recorded Temperatures and Refrigerator Setting 21

4. (a) Schematic of 5.8 cm Engine 24
   (b) Schematic of 5.8 cm Engine 24

5. Engine Structure 24

6. (a) Assembled 9.3 cm Engine With Cooling Jacket 24
   (b) Photo of the 5.8 cm Engine 24

7. Heat Engine Experiment 26

8. (a) Schematic of Open-End System 27
   (b) Schematic of Closed-End System 27

9. (a) Open-End System 28
   (b) Closed-End System 28

10. (a) Open-Ended Refrigerator 29
    (b) Closed-Ended Refrigerator 29

11. Temperature Profile for 5.8 cm Engine 31

12. Pressure Profile for 5.8 cm Engine 32

13. Variation of Temperature Difference for 5.8 cm Engine 32

14. Pressure Variation for 5.8 cm Engine 32

15. Acoustic RMS Pressure with the Change in Temperature Difference Across the Stack 34

16. Temperature Profile for Steel Wool 35

17. Temperature Profile for RVC 100 PPI 35

18. Temperature Profile for RVC 80 PPI 35

19. Temperature Difference for RVC 100 PPI, 80 PPI, and Steel Wool for 5.8 cm Engine 36

20. Temperature Profile for 5.8 cm and 9.3 cm Engine with RVC 100PPI 39

21. Acoustic Pressure Profile for 5.8 cm and 9.3 cm engine with RVC 100PPI 39

22. Acoustic Pressure Error Measurements at Different Angles for 5.8 cm Engine 41

23. Frequency Profile for Stack at 13 cm 44

24. Temperature Difference for Stack Located at 7 cm 45

25. Temperature Difference for Stack Located at 9 cm 45

26. Temperature Difference for Stack Located at 11 cm 45

27. Temperature Difference for Stack Located at 13 cm 46

28. Temperature Difference for Different Stack Location at 3.5 kPa of RMS Pressure 46

29. Temperature Difference for Different Stack Location at 218 Hz 47

30. Repeatability Error for 218 Hz Signal and 3.5 kPa of RMS Pressure 48

31. Repeatability Error for 218 Hz Signal and Stack at 13 cm 48

32. Temperature Difference for Different Stack Material at 13 cm 50

33. Temperature Profile Recorded Every 15 Seconds 50

34. Temperature Profile Recorded Every 5 Seconds 51

35. Enthalpy Flow Across the Tube for a Close-Ended System 52

36. Temperature Difference for Stack Located at 6 cm 53

37. Temperature Difference for Stack Located at 7 cm 53

38. Temperature Difference for Stack Located at 8 cm 53

39. Frequency Profile for Stack at 6 cm 54

40. Enthalpy Flow Across the Tube for an Open-Ended System 55

41. Temperature Difference for Different Stack Position at 0.35 kPa of RMS Pressure 55

42. Temperature Difference for Different Stack Position at 330 Hz 56

43. Repeatability Error for 330 Hz Signal and 0.5 kPa of RMS Pressure 56

44. Repeatability Error for 330 Hz Signal and Stack at 6 cm 57

45. Temperature Difference for Different Stack Material at 6 cm 58

Chapter 1

Introduction

Introduction

1.1. Background

Thermoacoustics is a science and technology field that studies heat and sound interactions. Sound waves in any fluid consist of coupled pressure, motion, and temperature oscillations. When sound travels through a narrow channel, an oscillating heat flow between the fluid and the channel's wall becomes significant. Devices in which heat-sound interactions play an important role are known as thermoacoustic systems [1]. Audible sound temperature fluctuations are usually very small and normally not important. In the case of thermoacoustic engines, the combination of temperature gradient and special system geometry makes these temperature fluctuations important, since they can significantly amplify sound [2].

Thermoacoustic effects have been studied since the 19th century. One of the first observations was made in 1850 when Sondhauss recorded sound appearance in glassblower equipment [3]. The sound waves were produced when hot glass came in contact with a cool open ended glass tube. The frequency of the observed tonal sound was equal to the natural frequency of the tube [4]. Subsequently, other thermoacoustic findings soon followed. In 1859, Rijke noticed that placing hot gauze in the lower half of an open-ended tube created a similar pure tone where sound oscillations were varied by changing the gauze location along the tube. Rijke postulated that the expansion of air at the gauze and the contraction of cooling air toward the open end of the tube explained the sound generation [5]. Soon after these discoveries, Lord Rayleigh came up with an explanation of the thermoacoustic instabilities which caused this phenomenon: "If heat be given to the air at the moment of greatest condensation, or be taken from it at the moment

of greatest rarefaction, the vibration is encouraged. On the other hand, if heat be given at the moment of greatest rarefaction, or abstracted at the moment of greatest condensation, the vibration is discouraged" [6].

Thermoacoustic devices can be made without moving parts and using various gases as working fluids. The simplicity of manufacturing such engines results in low cost and low maintenance and, therefore, is desirable in industry [7]. Thermoacoustic engines can be divided into two major groups. In the first group, thermoacoustic prime movers convert some fraction of heat supplied from a high temperature source into acoustic power, rejecting the rest of the heat into a low temperature heat sink. In the second group, thermoacoustic refrigerators and heat pumps use sound to pump heat against a temperature gradient. The temperature gradient in a refrigerator is typically much lower than in the heat engine [16]. Figure 1 shows the two basic types of heat engines.

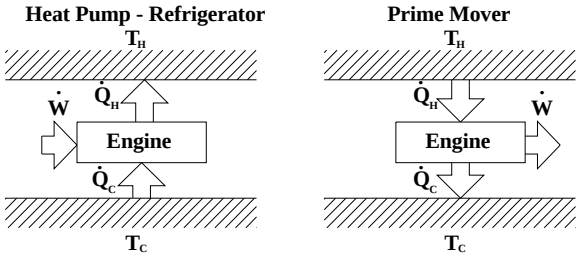

Figure 1: Two types of heat engine.

There have been major developments and advances in the thermoacoustic field in recent decades and some thermoacoustic systems have been tested for industrial use. One example is large scale commercial refrigeration using thermoacoustic engines. The efficiency limitations in simple standing wave engines motivated the development of closed loop traveling wave engines, a few meters in size, that produce approximately 1 kW of acoustic power [13]. Other medium-scale systems were built that produce up to

100 W of acoustic power. One example of such a thermoacoustic engine was built by NASA with a total length of 16 cm and weight of about 900 g [12].

Because manufacturing macro-scale thermoacoustic engines is relatively simple, most of the work and studies done use large or medium engines. Some of the thermoacoustic projects are aimed at converting acoustic power into electric power. A project attempting to facilitate this conversion was originally designed for a space generator which produced 100 W of electrical power at 20% efficiency. This engine has a total length of 16 cm, but the generated power is much larger in comparison to previous designs [14]. Another case study was done at Los Alamos National Laboratory that coupled a thermoacoustic engine to an electric alternator, which was part of a NASA space project [16].

1.1.1. Heat Engine

A simple thermoacoustic engine consists of a tube (resonator) with one end closed and the other end open to the atmosphere with a porous material, referred to as a stack, placed inside the tube at a fixed location. The system produces sound only when the temperature difference across the stack exceeds a critical value. Thermoacoustic heat engines can be divided in two major categories: standing-wave and traveling-wave engines. In a standing-wave thermoacoustic heat engine, heat is supplied to the oscillating gas at high pressure and is removed at a low pressure supporting pressure and velocity fluctuations. These self-sustained oscillations satisfy Rayleigh's criterion; in other words, heat is added to the gas in phase with pressure fluctuations, similar to the Stirling cycle [16]. For thermoacoustic pumps or refrigerators this process is reversed.

In a traveling-wave heat engine, the pressure and velocity components of an acoustic traveling wave are inherently phased to cause the fluid in the stationary temperature gradient to undergo a Stirling thermodynamic cycle. This cycle results in amplification or attenuation of the wave depending on the wave direction relative to the direction of the gradient. This cycle pumps heat in the direction opposite the direction of wave propagation through the device [9].

Various thermoacoustic systems have been built in the past, usually in large or medium scale. The main motivation for our research is to build a miniature engine with a relatively simple design for ease of manufacturing. An example of a relatively small thermoacoustic engine previously developed is a 14 cm Hofler tube [7]. The Hofler tube has a constant bore capped at one end, and similar to other engines, open on the other end. The open end is made of aluminum and funnel shaped with a stack of reticulated vitreous carbon (RVC). Smaller engines, down to few centimeters in length, were also built [17], but their design was not documented in details sufficient for reproduction.

1.1.2. Refrigerator

A simple thermoacoustic refrigerator consists of a resonator with one end attached to a speaker. The other end is open or closed, and porous material (stack) is placed at a certain location inside the resonator [6]. The stack usually consists of a large number of closely spaced surfaces aligned with the resonator tube. The primary constraint in selecting the stack is the fact that stack layers need to be placed a few thermal penetration depths apart. About four thermal penetration depths is the recommended plate separation in standing-wave systems. Thermal penetration depth is the distance, or thickness, of the

layer where unsteady heat propagates during one oscillation cycle [1]. In a refrigerator, externally applied work transfers heat from the lower temperature reservoir to the higher temperature reservoir. In this case the external work is supplied by the standing sound wave produced by a speaker in the resonator. The standing sound wave forces the gas particles to oscillate parallel to the walls of the stack. The alternating compression and rarefaction of the gas causes the local temperature of the gas to fluctuate. If the local temperature of the gas becomes higher than that of the nearby stack wall, heat is transferred from the gas to the stack wall. However, if the local temperature of the gas drops below that of the stack wall, heat is transferred from the wall to the gas. Depending on the system's configuration, the mean temperature of each stack end will differ. In the closed-end configuration, the temperature of the stack end close to the cap is higher than the other end of the stack, where a cooling effect is achieved. The heat is pumped from the cold end to the hot end.

1.2. Objectives

The main objective of this study is to build and test a miniature thermoacoustic engine and quantify its performance. The development process included several different models that were built and tested. The heat engine was tested with different stack materials in order to find the best material for the stack. The values measured in our studies are the critical temperature across the stack and the pressure amplitude of the sound produced. These values are compared with theoretical values obtained from numerical analysis.

The second part of our efforts deals with a construction of a cooling model with a speaker as a sound source. This system is built and then tested with different stack materials and two different geometry configurations: closed- and open-ended. The frequency of the acoustic signal and the pressure amplitude inside the resonator were controlled parameters, and the measured parameter was the temperature difference across the stack. These studies are done to identify the differences between a closed and open systems and also to find the most effective system. The experimental results were compared with the theoretical values. Some results of these activities were presented at conferences [18, 19].

Chapter 2

Methodology

2. Methodology

2.1. Theoretical Formulation

2.1.1. Heat Engine

The goal of this section is to theoretically obtain the critical temperature difference across the stack, the acoustic power produced, and the acoustic pressure amplitude. In order to formulate necessary equations to calculate these parameters, the conservation of energy in the system is analyzed. Figure 2 shows a configuration of our acoustic engine and the acoustic pressure and velocity waveforms. The acoustic pressure is maximized at the closed-end and zero at the open end. The acoustic velocity distribution starts at zero at the closed end and reaches a maximum value at the open end. Figure 2 (a) and (b) show the most important dimensions of the thermoacoustic heat engine.

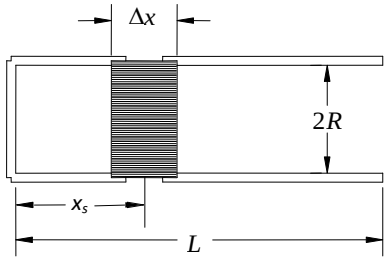

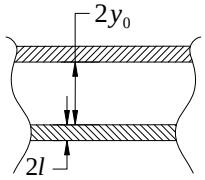

Figure 2. (a) Schematic of thermoacoustic engine **(b) Expanded view of the stack plates**

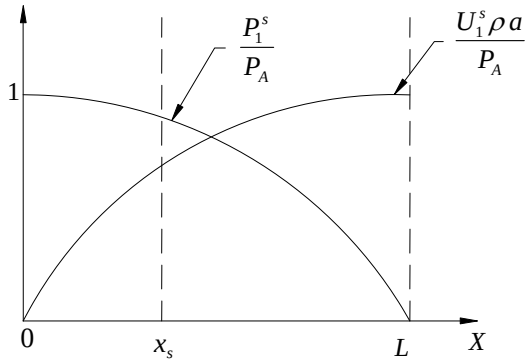

(c) Pressure and velocity waveforms along the resonator.

The pressure and velocity components of the standing acoustic wave in the resonator are functions of time t and distance x:

$$p_1 = p_1^s(x)e^{i\omega t}, \tag{1}$$

$$u_1 = \frac{u_1^s}{i}(x)e^{i\omega t}, \tag{2}$$

The spatial component of the acoustic standing wave pressure and velocity are approximated as follows:

$$p_1^s(x) = P_A \cos\left(\frac{x}{\lambda_{rad}}\right), \tag{3}$$

$$u_1^s(x) = \left(\frac{P_A}{\rho_m a}\right)\sin\left(\frac{x}{\lambda_{rad}}\right). \tag{4}$$

The closed end location is selected to be at zero and the x-axis is directed toward the open end. In figure 2 the spacing and the thickness of the plates are shown. Half-spacing between the plates is y_0 and half-plate thickness is l. In figure 2, X_S is the distance from closed end to the middle of the stack. The pressure and velocity waveforms are functions of x and vary along the engine.

The radian wavelength of the fundamental acoustic wave in the open-closed tube is approximated as follows:

$$\lambda_{rad} = \frac{a}{\omega} = \frac{\lambda}{2\pi} = \frac{2L}{\pi}. \tag{5}$$

The wavelength λ is a function of length of the resonator. In our case, since one end of the engine is open, the wave length is equal to about $4L$. The speed of sound is a function of temperature and for ideal gas can be written as follows:

$$a = \sqrt{\gamma RT}\,, \tag{6}$$

where T is the gas temperature.

Therefore the natural frequency of the open-closed tube becomes a function of temperature and tube length:

$$f = \frac{\omega}{2\pi} = \frac{\sqrt{\gamma RT}}{4L}\,, \tag{7}$$

In order to find the critical temperature difference across the stack we use the energy balance of the system [3]:

$$\dot{W}_2 = \dot{E}_{rad} + \dot{E}_{res} + \dot{E}_{hx}\,, \tag{8}$$

where $\dot{W}_2$ is the acoustic power produced, $\dot{E}_{rad}$ is the radiated acoustic power, $\dot{E}_{res}$ is the acoustic power absorbed by the walls of the resonator, and $\dot{E}_{hx}$ is the acoustic power absorbed by thermoviscous effects in heat exchangers.

Acoustic oscillations occurring in the vicinity of a plate result in two important effects: the generation and absorption of acoustic power $\dot{W}_2$, and also a time-average heat flow $\dot{Q}_2$ near the surface of the plate, both effects occurring along the direction of acoustic oscillation.

Now each term in the energy balance equation will be analyzed. The acoustic power produced in the presence of thermoviscous losses can be written as follows [3]:

$$\dot{W}_2 = \left(\frac{1}{4}\Pi\delta_k \Delta x \frac{(\gamma-1)\omega\left(p_1^s(x_S)\right)^2}{\rho_m a^2(1+\varepsilon_s)}\right)\left(\frac{\Gamma}{\left(1+\sqrt{\sigma}\right)\left(1-\frac{\delta_\nu}{y_0}+\frac{\delta_\nu{}^2}{2y_0{}^2}\right)}-1\right)-\frac{1}{4}\Pi\delta_\nu\Delta x\frac{\omega\rho_m\left(u_1^s(x_s)\right)^2}{1-\frac{\delta_\nu}{y_0}+\frac{\delta_\nu{}^2}{2y_0{}^2}}, \quad (9)$$

The flow velocity through the stack will be different due to finite thickness of stack plates. In order to have continuous flowrate throughout the system, a correction factor must be added to the velocity component throughout the stack. The velocity distribution along the stack becomes:

$$u_1^s(x) = \left(\frac{P_A}{\rho_m a}\right)\left(1+\frac{l}{y_0}\right)\sin\left(\frac{x}{\lambda_{rad}}\right). \quad (10)$$

All symbols in equation (9) are explained below or given in nomenclature.

Since the pressure amplitude and temperature difference are the target parameters. This way the acoustic power equation can be written in simplified form as follows [3]:

$$\dot{W}_2 = C_1 P_A^2(\Delta T - C_2) - C_3 P_A^2. \quad (11)$$

where C_1, C_2, and C_3 are the constants.

Since the working space in the engine is bounded by the walls of the resonator and the air is a viscous fluid, the viscous penetration depth and the thermal penetration depth play a critical role in our calculations. The thermal penetration depth is the distance through which the heat can be diffused through the working fluid, in our case air, during time interval equal to $\frac{2\pi}{\omega}$. On the other hand, the air will move without heat transfer when it is sufficiently far from the wall. The acoustic oscillations of the air in the engine result in viscous shear stresses that lead to attenuating loss mechanism that occurs in the volume

of air generally within a viscous penetration depth**.** The viscous penetration depth in the fluid can be written as follows:

$$\delta_\nu = \sqrt{\frac{2\nu}{\omega}}, \tag{12}$$

where kinematic viscosity is:

$$\nu = \frac{\mu}{\rho_m}. \tag{13}$$

Here the mean density ρ_m is a function of temperature that for the ideal gas becomes:

$$\rho_m = \frac{P}{R_g T}, \tag{14}$$

where for air $R_g = 0.287 \frac{kJ}{kg\,K}$.

The dynamic viscosity of the working fluid, in our case the air, also varies with temperature [3].

The thermal penetration depth of the solid is

$$\delta_k = \sqrt{\frac{2k}{\omega}}, \tag{15}$$

where thermal diffusivity is

$$k = \frac{K}{\rho_m c_p}. \tag{16}$$

The Prandtl number is one of the parameters used, which can be written as:

$$\sigma = \frac{c_p \mu}{K} = \frac{\nu}{k} = \left(\frac{\delta_\nu}{\delta_k}\right)^2. \tag{17}$$

The plate heat capacity ratio ε_s uses the properties of the fluid, in our case the air, and the properties of the solid. Considering $y_0 >> \delta_k$ and $l >> \delta_s$, the simplified expression for ε_s is:

$$\varepsilon_s = \frac{\rho_m c_p \delta_k^{\ air}}{\rho_s c_s \delta_s^{\ solid}}, \tag{18}$$

The perimeter in equation (9) can be approximated assuming parallel plate stack geometry:

$$\Pi = \frac{\pi D^2}{2h}, \tag{19}$$

where $h = 2y_0$, if $l << y_0$, or with the finite plate thickness, $h = 2y_0 + 2l_0$.

The next term that appears in the equation is the normalized temperature gradient. Normalized temperature gradient is the ratio of to the actual and ideal critical temperature gradient.

$$\Gamma = \frac{\nabla T_m}{\nabla T_{crit}}, \tag{20}$$

where ∇f is defined as $\frac{df}{dx}$ since we consider a one-dimensional problem.

In this case ∇T_m is the mean temperature gradient of the tube in the x-direction, which can be represented as follows:

$$\nabla T_m = \frac{\Delta T}{\Delta x}, \tag{21}$$

where ΔT is the difference temperature of two sides of the stack and Δx is the stack length.

The ∇T_{crit} is the critical mean temperature gradient that can be obtained using the following equation [3]:

$$\nabla T_{crit} = \frac{T_m \beta \omega p_1^s(x_S)}{\rho_m c_p u_1^s(x_s)}. \tag{22}$$

The thermal expansion coefficient β for an ideal gas is

$$\beta = \frac{1}{T}. \tag{23}$$

Now we consider individual terms on the right hand side of equation (8).

The first term is the radiated acoustic power $\dot{E}_{rad}$. The acoustic power radiating away from the open end of a small-diameter $\frac{\lambda}{4}$ resonator [1]:

$$\dot{E}_{rad} = \left(\frac{\pi}{8}\right)\left(\frac{P_A^2 R^4}{\rho_m a \lambda_{rad}^{\ 2}}\right), \tag{24}$$

Where P_A is the acoustic pressure amplitude at the closed end of the resonator and R is the radius of the resonator. The simplified form of radiated acoustic power is:

$$\dot{E}_{rad} = C_4 P_A^2, \tag{25}$$

where

$$C_4 = \left(\frac{\pi^3 R^4}{32 \rho_m a L^2}\right). \tag{26}$$

Acoustic power adsorbed by the resonator walls $\dot{E}_{res}$ is obtained by integrating the local power attenuation per surface area over $\frac{\lambda}{4}$ of side walls:

$$\dot{e}_{res} = \frac{\delta_k \left(p_1^s\right)^2}{4 \rho_m a^2} \frac{\omega(\gamma - 1)}{1 + \varepsilon_s} + \frac{1}{4} \rho_m \left(u_1^s\right)^2 \delta_v \omega, \tag{27}$$

where p_1^s and u_1^s were defined by equation (3) and (4).

We integrate $\dot{e}_{res}$ over the surface area of the resonator.

$$\dot{E}_{res} = \int_0^L (\dot{e}_{res}) 2\pi R\, dx + \pi R^2 \dot{e}_0 . \tag{28}$$

Performing the integration we obtain:

$$\dot{E}_{res} = \left(\frac{RL\pi\omega P_A^2}{4a^2\rho_m} \right) \left(\frac{\gamma - 1}{1+\varepsilon_s} \delta_k \left(1 + \frac{R}{L} \right) + \delta_\nu \right). \tag{29}$$

The simplified equation of the acoustic power adsorbed is:

$$\dot{E}_{res} = C_5 P_A^2 , \tag{30}$$

where

$$C_5 = \left(\frac{RL\pi\omega}{4a^2\rho_m} \right) \left(\frac{\gamma - 1}{1+\varepsilon_s} \delta_k \left(1 + \frac{R}{L} \right) + \delta_\nu \right). \tag{31}$$

We obtain the acoustic power absorbed by viscous effects in the heat exchanger $\dot{E}_{hx}$ by using the same equation that the acoustic power absorbed but this time it will be multiplied the surface area of the first and the second heat exchanger.

Acoustic power absorbed:

$$\dot{E}_{hx} = \left[\frac{\delta_k \left(p_1^s \right)^2}{4\rho_m a^2} \frac{\omega(\gamma - 1)}{1+\varepsilon_s} + \frac{1}{4} \rho_m \left(u_1^s \right)^2 \delta_\nu \omega \right] \Pi_{hx} \Delta x_{hx} , \tag{32}$$

where the surface area can be expressed as follows:

$$\Pi_{hx} \Delta x_{hx} = \frac{\pi D_{hx}^2}{2h_{hx}} \Delta x_{hx} = \frac{\pi D_{hx}^2}{2y_{0hx} + 2l_{hx}} \Delta x_{hx} . \tag{33}$$

In this case the pressure and velocity amplitude can be estimated from equations (3) and (4) at heat exchanger locations.

The total energy absorbed by both heat exchangers (on each side of stack) is:

$$\dot{E}_{hx} = \dot{E}_{hx1} + \dot{E}_{hx2}\,, \tag{34}$$

Finally the energy absorbed by the heat exchangers can be written as follows:

$$\dot{E}_{hx} = C_6 P_A^2\,, \tag{35}$$

where

$$C_6 = \frac{\omega \Pi_{hx} \Delta x_{hx}}{4\rho_m a^2}\left[\frac{A\delta_k(\gamma-1)}{1+\varepsilon_s} + B\delta_\nu\right], \tag{36}$$

where A and B are parameters that include the acoustic pressure and velocity:

$$A = \cos^2\left(\frac{\pi\left(x_s - \frac{\Delta x}{2}\right)}{2L}\right) + \cos^2\left(\frac{\pi\left(x_s + \frac{\Delta x}{2}\right)}{2L}\right), \tag{37}$$

$$B = \sin^2\left(\frac{\pi\left(x_s - \frac{\Delta x}{2}\right)}{2L}\right) + \sin^2\left(\frac{\pi\left(x_s + \frac{\Delta x}{2}\right)}{2L}\right). \tag{38}$$

Combining equations (11), (25), (30), and (35) the critical temperature difference across the stack ΔT can be written as follows:

$$\Delta T = \frac{C_3 + C_4 + C_5 + C_6}{C_1} + C_2\,. \tag{39}$$

It is important to note that the temperature difference is a function of geometry and material property of the stack. Material properties relates to thermo-physical properties of the materials used in the stack (air, copper, stainless steel). The geometries relate to the resonator length L and radius R, stack position x and length Δx, plate thickness $2l$ and spacing $2y_0$, and heat exchanger thickness $2l_{hx}$, spacing $2y_{hx}$, and length Δx_{hx}.

The acoustic pressure amplitude P_A in the exited region is another parameter that can be determined by modeling. The ΔT will be eliminated in order to solve for P_A, which is a function of geometry of the stack, material property, and the temperature difference outside heat exchangers ΔT_{ext}.

$$P_A = P_A\left(\Delta T_{ext}, geometry, material\,property\right)$$

Heat flux through the stack is as follows [3]:

$$\dot{H} = \left(-\frac{1}{4}\Pi\delta_v \frac{T\beta\, p_1^s(x_S)\, u_1^s(x_S)}{(1+\sigma)(1+\varepsilon_s)\left(1-\frac{\delta_v}{y_0}+\frac{{\delta_v}^2}{2{y_0}^2}\right)} \right)\left(\frac{\Gamma\left(\sigma\varepsilon_s - \frac{\delta_v}{y_0}\left(1+\sqrt{\sigma}\right)-\sqrt{\sigma}\right)}{1+\sqrt{\sigma}} \right) - \Pi\left(y_0 K + lK_s\right)\frac{\Delta T}{\Delta x}, \quad (40)$$

After inserting the values for pressure and velocity the equation becomes:

$$\dot{H} = P_A^2 A + B. \quad (41)$$

where

$$A = -\left(\frac{\Pi\Gamma\delta_v T\beta\left(\sigma\varepsilon_s - \frac{\delta_v}{y_0}\left(1+\sqrt{\sigma}\right)-\sqrt{\sigma}\right)\left(1+\frac{l}{y_0}\right)\cos\left(\frac{\pi x_s}{2L}\right)\sin\left(\frac{\pi x_s}{2L}\right)}{4\rho a\left(1+\sqrt{\sigma}\right)(1+\sigma)(1+\varepsilon_s)\left(1-\frac{\delta_v}{y_0}+\frac{{\delta_v}^2}{2{y_0}^2}\right)} \right), \quad (42)$$

$$B = -\frac{\Pi\Delta T\left(y_0 K + lK_s\right)}{\Delta x}, \quad (43)$$

In order to calculate the acoustic pressure amplitude we equate the heat flux through the stack $\dot{H}$ with the heat flux through either heat exchanger:

$$\dot{H} = K\frac{(\Delta T_{ext} - \Delta T)}{2}\left(\frac{S}{d}\right), \quad (44)$$

where $\dot{H}$ is the energy flux through either heat exchanger, K_{cu} is thermal conductivity of copper, S effective area, and d is the effective distance.

These parameters can be estimated as follows:

$$d = \frac{R_{hx}}{2} = \frac{D_{hx}}{4}, \tag{45}$$

$$S = 2nl_{hx}\Delta x_{hx}, \tag{46}$$

where

$$n = \frac{\pi R_{hx}}{\left(l_{hx} + y_{0hx}\right)}. \tag{47}$$

The heat flow through the heat exchanger can now be written as:

$$\dot{H}_{hx} = C\left(\Delta T_{ext} - \Delta T\right), \tag{48}$$

where

$$C = \frac{4nK_{cu}l_{hx}\Delta x_{hx}}{D_{hx}}. \tag{49}$$

Pressure amplitude can be calculated equating the heat transfer equations:

$$P_A = \sqrt{\frac{C\left(\Delta T_{ext} - \Delta T\right) - B}{A}}. \tag{50}$$

2.1.2. *Refrigerator*

In the case of the cooling demonstrator, the main parameters are the temperature difference across the stack and acoustic pressure amplitude inside the resonator. In this section, conservation of energy is used to develop all the formulas necessary for both open-end and closed-end systems. The results will be different since the boundary conditions are different. Therefore, not only the temperatures of each end of the stack will be different, but also the acoustic pressure and velocity distributions will have different forms.

The pressure and velocity components of the acoustic wave in the resonator for an open-end cylindrical tube are functions of time t, distance x, frequency of the signal [1]:

$$p_1 = p_1^s e^{i\omega t} = P_A e^{i\omega t}\left(\frac{\sin\left(\frac{2\pi f(l-x)}{a}\right)}{\sin\left(\frac{2\pi f l}{a}\right)}\right), \tag{51}$$

where

$$k = \frac{\omega}{a} = \frac{2\pi f}{a}\ , \tag{52}$$

$$u_1 = iu_1^s e^{i\omega t} = \left(\frac{P_A e^{i\omega t}}{iZ_0}\right)\left(\frac{\cos\left(\frac{2\pi f(l-x)}{a}\right)}{\sin\left(\frac{2\pi f l}{a}\right)}\right), \tag{53}$$

$$Z_0 = \rho_{air} a\,, \tag{54}$$

where a is the speed of sound, k is the wave number, and Z_0 is the acoustic impedance.

For the refrigeration system the equation for thermoacoustic heat pumping can be written as follows [1]:

$$\dot{H}_2 = -\frac{1}{4}\Pi\delta_k \frac{T_m \beta p_1^s \left\langle u_1^s \right\rangle}{(1+\varepsilon_s)(1+\sigma)\left(1-\frac{\delta_\nu}{y_0}+\frac{\delta_\nu^2}{y_0^2}\right)} \times$$

$$\left[\Gamma\frac{1+\sqrt{\sigma}+\sigma+\sigma\varepsilon_s}{1+\sqrt{\sigma}} - \left(1+\sqrt{\sigma}-\frac{\delta_\nu}{y_0}\right)\right], \tag{55}$$

where p_1^s and u_1^s can be estimated using equation (51) and (53),

$$\Gamma = \frac{\nabla T_m}{\nabla T_{crit}}, \tag{56}$$

$$\nabla T_m = \frac{T_t - T_b}{\Delta x}, \tag{57}$$

where T_b is the temperature of the bottom of the stack close to the speaker, T_t is the temperature of the top of the stack close to end of the resonator, and x_s is the distance from the source to the center of the stack. The position of microphone depends of the configuration. For the closed- and open-end systems this parameter is different.

In figure 3 the configuration of the refrigerator is represented:

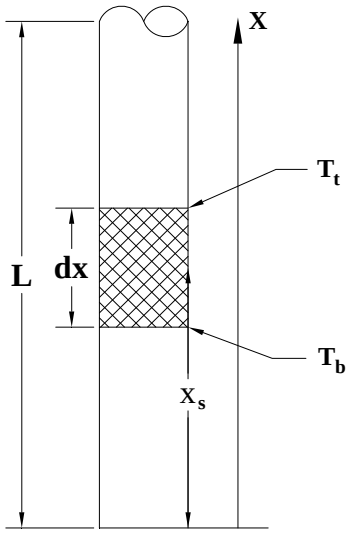

Figure 3: Locations of recorded temperatures and refrigerator setting.

Using equation (51) we solve for P_A, the pressure amplitude inside the resonator.

$$P_A = \frac{p_1^s(x_m)\sin\left(\frac{2\pi f l}{a}\right)}{\sin\left(\frac{2\pi f (l-x)}{a}\right)}, \tag{59}$$

where $p_1^s(x_m)$ is the pressure amplitude at the microphone location x_m.

We aim at the qualitative comparison of test data and theoretical results.

Since the direction of the heat pumping is our main objective, the above formula can be simplified as follows:

$$H_2 \sim h_2, \tag{60}$$

$$h_2 = p_1^s(x_s)u_1^s(x_s). \tag{61}$$

For a closed ended system spatial variations of acoustic pressure and velocity are:

$$p_1^s(x) = \left(\frac{(\rho a)^2 P_A}{\sin\left(\frac{2\pi f l}{a}\right)} \right) \cos\left(\frac{2\pi f (l-x)}{a} \right), \tag{62}$$

$$u_1^s(x) = \rho a P_A \left(\frac{\sin\left(\frac{2\pi f (l-x)}{a}\right)}{\sin\left(\frac{2\pi f l}{a}\right)} \right), \tag{63}$$

For estimating the thermoacoustic enthalpy flow, equations (60) and (61) can be used for the closed-end system as well.

2.2. Experimental Setups

2.2.1. Heat Engine

The resonator of the engine consists of three parts. The first part is the tube with one end closed acting as the hot heat exchanger in the system. It is made of solid copper tubing, which was machined down to appropriate dimensions. The second part is the ceramic stack holder that contains a cavity with the same inner diameter as the copper tube. The third part is the open-end tube made of copper and similarly machined to the right dimensions. Flanges were added to each part, which were connected with each by long screws tightened with nuts for the integrity of assembly. The heat exchangers were two layers of thin copper mesh placed on each side of the stack. The assembled engine is schematically shown in figure 5. The materials used for the stack were similar to the Hofler tube [7]: Reticulated Vitreous Carbon foam (RVC) with two different densities and a steel wool. RVC is a porous structure or open-celled foam consisting of an interconnected network of solid fibers. RVCs can be specified with two different characteristics: the number of pores per inch (PPI) and volumetric porosity [8]. The RVCs used in our test are 100 PPI and 80 PPI. The main dimensions of the two engines used in this experiment are identical except for the total length, which are 5.8 and 9.3 cm. Since the geometry and material properties of each part of the engine are the variables that could change the results, the two arbitrary lengths were chosen to investigate the change in results with the change in geometry. The inner diameter of the copper tubes and the stack holder is 1.4 cm. The copper tubes have a 0.05 cm wall thickness. The stack length is 0.7 cm and is located 1.6 cm away from the closed end. In figure 4 (a) and (b) the two engines are shown with their respective dimensions.

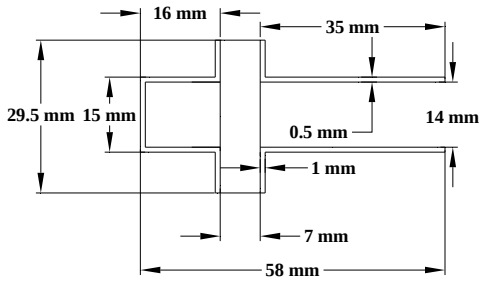

Figure 4: (a) Schematic of 5.8 cm engine.

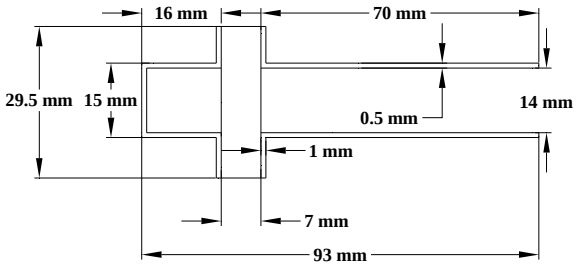

(b) Schematic of 9.3 cm engine.

The following figure shows the engine structure emphasizing all the parts in the heat engine.

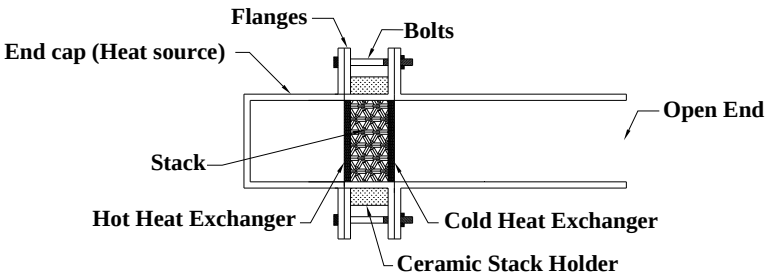

Figure 5: Engine structure.

Figure 6 (a) and (b) show pictures of the heat engine with and without the cooling jacket. In order to create a tight vessel with the exception of the open end, graphite gaskets that resist temperatures up to 455°C were placed between flanges of the engine parts.

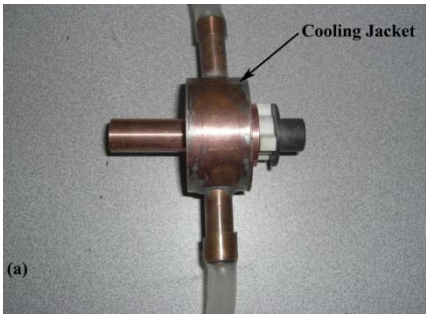

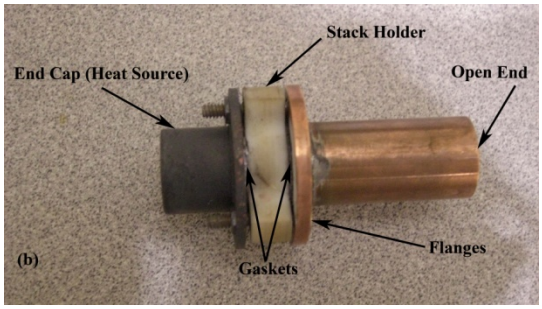

Figure 6: (a) Assembled 9.3 cm engine with the cooling jacket. (b) Photo of the 5.8 cm engine.

To achieve the critical temperature difference across the stack, the closed end is heated using a butane torch, and the opposite end of the stack is cooled with the cooling water. A cooling jacket was fabricated to fit over the open-end tube. Using a cold-water bath and a circulator, water at approximately 1°C is pumped through the jacket. The design of the stack holder was chosen to reduce its cross-sectional area and heat transfer between the hot and cold sections.

Two K-type thermocouples were inserted between the flanges and gaskets on each side of the stack for recording the temperatures of the hot and cold ends of the stack. A LinearX M52 microphone was placed outside the engine for measuring the acoustic pressure amplitude. This particular microphone is a high-performance low-voltage condenser type. It is specifically designed for the measurement of high sound pressure levels. The microphone conforms to the external dimensions of industry standard 1/2 inch measurement microphones. It has 170dB SPL capability, wide frequency response, low voltage power supply requirements, and a sensitivity of 1.2 $\frac{mV}{\mathrm{Pa}}$. The acoustic pressure was measured using a microphone 30 cm away from the open end. The reason for measuring at this distance was to avoid changes in boundary conditions at the open end of the engine, and to provide an approximation to treat the open end as a point acoustic source. A sound level meter was also used at the same distance for comparison. Figure 7 shows the setting of the experiment. Since under these conditions the sound produced will be reflected from other surfaces present in the room, such as the walls, ceiling, the table, and other objects, the measured values may contain a large margin of error. The microphone is 171 cm away from the left wall, about 400 cm away from the right wall, and about 80 cm away from the back wall. The distance from ceiling to the microphone is

about 15 m and from the microphone to the ground is about 130 cm. The distance to the table is about 26 cm where soft foam was placed on for acoustic damping. Under these specific conditions the acoustic pressure was measured.

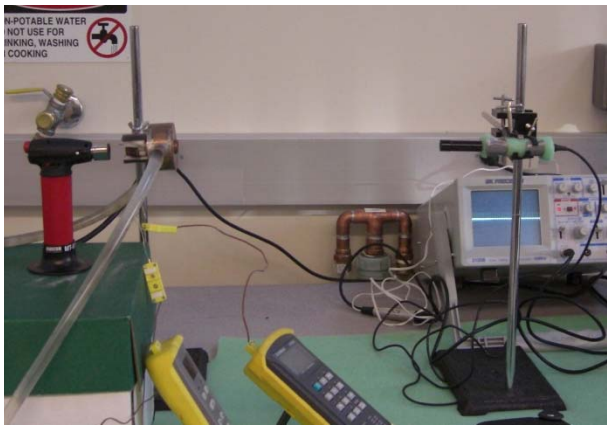

Figure 7: Heat engine experimental setup.

2.2.2. Refrigerator

The refrigerator is driven by a 100 W RCA 4” 2-way full range speaker made by Smart Mobile Technology. The speaker is mounted to a 5 cm thick plastic plate. This plate has a hole with the size of the speaker to allow vertical movement of air. A 1 cm thick plastic plate, with a hole in the center the same size as the resonator, is screwed to the 5 cm plate, and an acrylic tube is inserted in the thinner plate. For the open end, the resonator is 17.5 cm long with an internal diameter of 3 cm. In the case of the closed end, the length of the tube is 29 cm so that a cap can be screwed on top, but the inner diameter was machined to be the same. Figure 8 shows a representation of both systems with all parts and main dimensions.

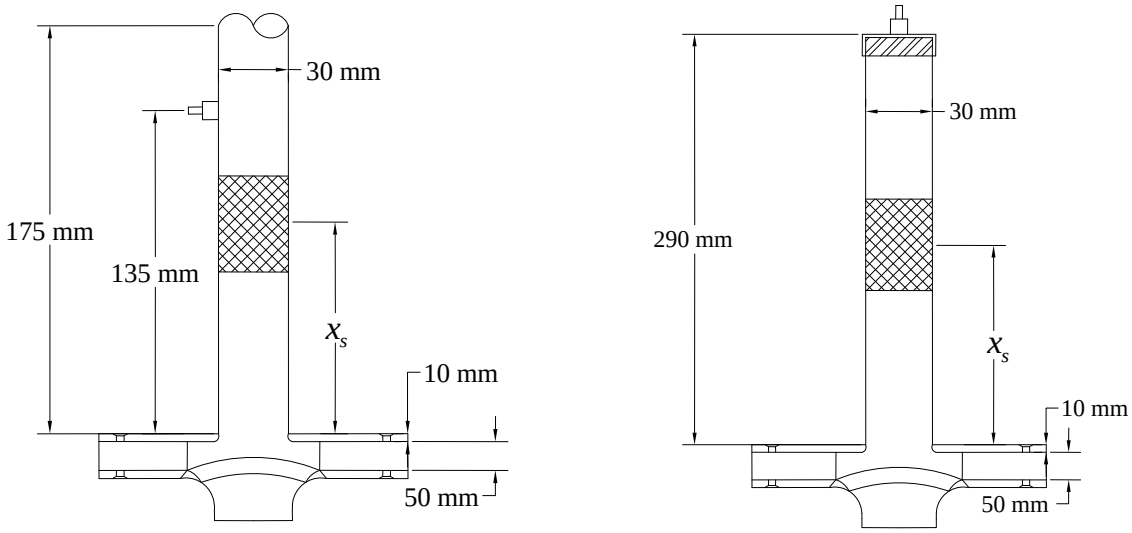

Figure 8: (a) Schematics of open-end system. **(b) Schematic of closed-end system**

For each configuration, different types of stacks were tested in order to find the most efficient stack for each system. The stack materials included cotton wool, steel wool with two different densities, and ceramics with two different porosities. The steel wool is a bundle of strands of very fine soft steel filaments with a fiber diameter of 50 μm for super-fine and 80 μm for fine wool. This particular steel wool is a production of Rhodes American Steel Wool. The two grades that responded to our system were the super fine and extra fine. The Celcor cellular ceramic substrates used in our experiment are made by Corning Incorporated and they have been widely used at the core of the catalytic converters. The ceramic substrates have high temperature durability and can effectively operate at temperatures up to 1200 °C. Their single piece structure and cellular geometry ensure stiffness and mechanical durability. The particular ceramic used in these experiments has a porosity of 35% [20]. The ceramic structure is parallel plates that are placed vertically, creating square shaped gaps. These squares have a side length of approximately 1 mm. For our system the best results were obtained using the super-fine

steel wool. The following figure 9 (a) and (b) shows the structure of both closed- and open-end refrigerator with all the components.

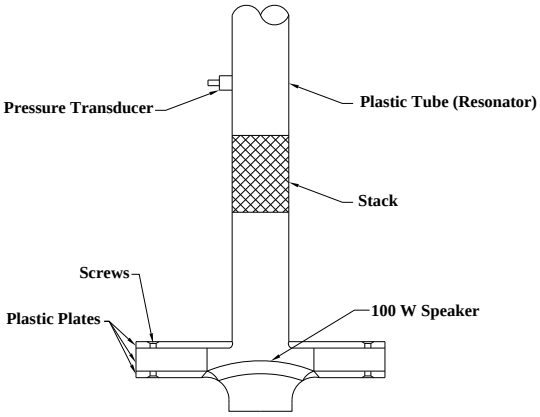

Figure 9: (a) Open-end system.

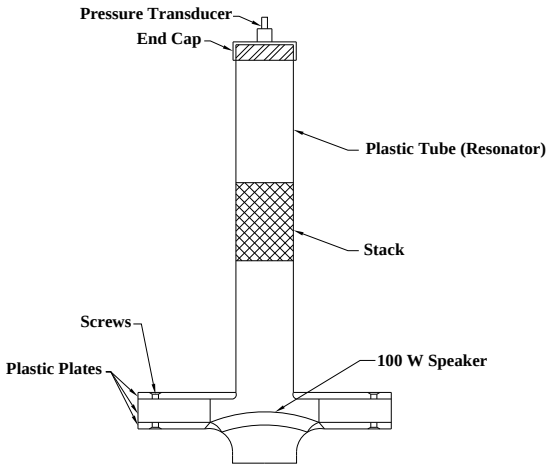

(b) Closed-end system.

Signal from a function generator is amplified and delivered to a speaker that produces sound. Since the resonators are detachable from the base, the same speaker is used for both closed and open ended systems. In order to measure the pressure amplitude inside the resonator during operation, a pressure transducer is mounted to the resonator tube at a set location shown in figure 9. The transducer is an 8510C-15 Endevco Piezoresistive pressure transducer with a sensitivity of 2.04 $\frac{\text{mV}}{\text{Pa}}$ and a range from 0 to 103.4 kPa. Because of the different settings the location of the transducer is different. The pressure transducer captures the signal and sends it to an amplifier, which is connected to an oscilloscope. Utilizing the graphical results of a 2120B BK Precision dual trace oscilloscope, the signal can be analyzed to determine the frequency and the pressure amplitude during operation. In figure 10 (a) and (b) show a picture of both systems during operation.

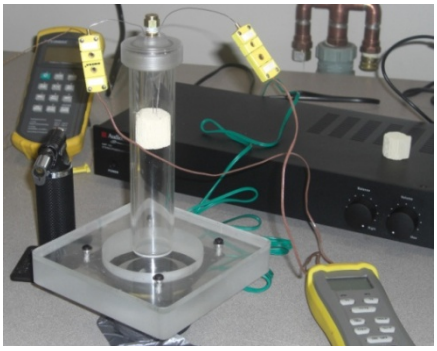

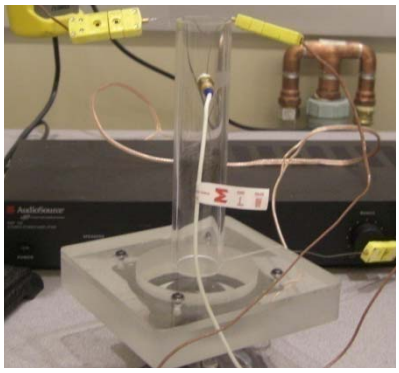

Figure 10: (a) Closed-ended refrigerator. **(b) Open-ended refrigerator.**

Chapter 3

Results and Discussion

3. Results and Discussions

In this section all the experimental results for both heat engine and refrigerator are presented, discussed and compared to theoretical results.

3.1. Heat Engine

It was very important to reach the critical temperature difference in order for the system to respond and produce sound. The following figures are the results of the 5.8 cm engine and RVC 100 PPI. In figure 11 the recorded temperatures over a period of time are presented. As we can see the engine produced a sound in approximately one minute after the torch was turned on, when the temperature difference across the stack sound appears in the range $\Delta T = 300-350°C$.

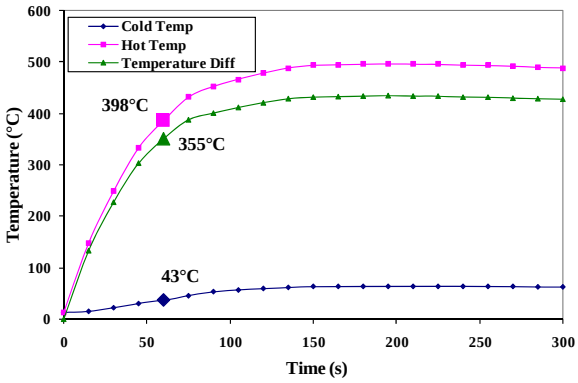

Figure 11: Temperature profile for 5.8 cm.

Another important measurement in our heat engine was the sound pressure produced, which is presented in figure 12.

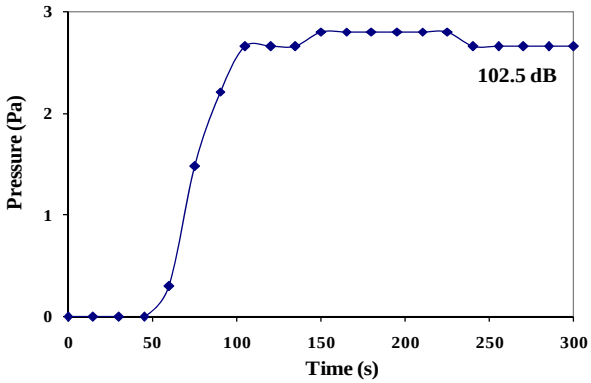

Figure 12: Pressure profile for 5.8 cm engine.

Uncertainty analysis was done for this configuration in order to identify the repeatability error. In figure13 the repeatability error for the temperature difference across the stack after 60 s and 150 s is shown. In figure 14 the uncertainty for the pressure measurements is represented. The uncertainty calculations made in this section is specific for the setup and environment that the test were carried. These uncertainties do not apply in any other conditions and configurations.

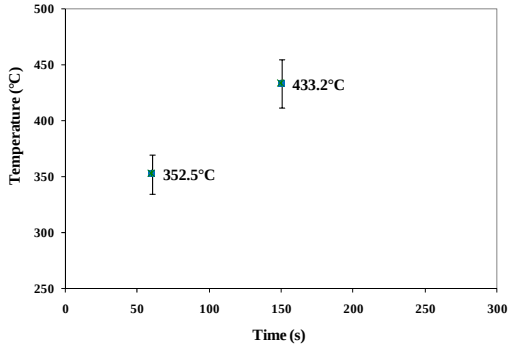

Figure 13: Variation of temperature difference for 5.8 cm engine.

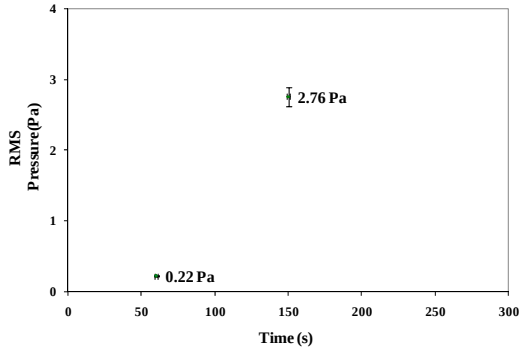

Figure 14: Pressure variation for 5.8 cm engine.

Time (s)	60	150
T_1 (°C)	350	433
T_2 (°C)	359	431
T_3 (°C)	343	443
T_4 (°C)	353	426
T_5 (°C)	366	431
T_6 (°C)	343	429
T_7 (°C)	350	428
T_8 (°C)	356	432
T_9 (°C)	348	440
T_{10} (°C)	357	439
Avg. Temp. (°C)	352.50	433.20
Linearity (°C)	0.7	0.7
Thermocouple Sensitivity (°C)	0.35	0.35
Thermometer Sensitivity (°C)	2.06	2.30
Zero Shift (°C)	0.50	0.50
Standard Dev. (°C)	7.23	5.61
Standard Dev. of Mean (°C)	2.29	1.78
Total Bias (°C)	2.26	2.48
Total Uncertainty (°C)	5.10	4.33

Table 1: Tabulated temperature uncertainty calculations.

Time (s)	60	150
P_1 (Pa)	0.2	2.8
P_2 (Pa)	0.1	2.8
P_3 (Pa)	0.3	2.8
P_4 (Pa)	0.3	2.65
P_5 (Pa)	0.3	2.8
P_6 (Pa)	0.2	2.65
P_7 (Pa)	0.1	2.8
P_8 (Pa)	0.2	2.8
P_9 (Pa)	0.1	2.65
P_{10} (Pa)	0.4	2.8
Avg. Acoustic Pressure (Pa)	0.22	2.76
Oscilloscope Readability error (Pa)	0.09	0.09
Microphone Sensitivity (Pa)	0.018	0.23
Standard Dev. (Pa)	0.10	0.07
Standard Dev. of Mean (Pa)	0.03	0.02
Total Bias (Pa)	0.09	0.25
Total Uncertainty (Pa)	0.23	0.25

Table 2: Tabulated pressure uncertainty calculations.

In figure 15 the pressure amplitude of the system is plotted against temperature difference across the stack. Here we can see that after reaching certain temperature at the hot end of the engine, in this case 500 °C, the system reaches steady state and the change in pressure amplitude is not drastic. From the time the sound produced to the time the sound reaches maximum amplitude is about 135 s. The recorded temperature of the heat

source, at the closed end was about 398 °C when the sound was produced, and it increased up to 500 °C when the system was in steady state. The cold-open end was about 36 °C and in steady state reached approximately 65 °C. As a result, the temperature difference across the stack was 350 °C at the start and reached 430 °C in equilibrium. In these conditions, the RMS acoustic pressure for the 5.8 cm engine was about 2.7 Pa, which is equivalent to 102 dB sound pressure level. The frequency of the sound produced was about 1.4 kHz at equilibrium. In this case the stack used was RVC 100 PPI.

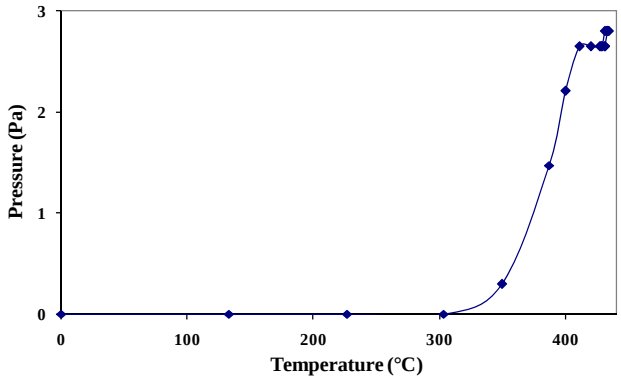

Figure 15: Acoustic RMS pressure with the change in temperature difference across the stack.

The same process was repeated for the 5.8 cm engine with different stacks. As mentioned before, the only other stacks that responded where the RVC 80 PPI and steel wool. When the engine produced sound, the acoustic pressure amplitude and the frequency of the system were relatively similar. The only difference was in the time required for the engine to produce sound and the critical temperature difference across the stack. In figure 16, 17 and 18 the temperature profile between the 5.8 cm engine with RVC 100 PPI, RVC 80 PPI and super fine steel wool are presented. The temperature differences at which the engine started to produce sound are marked in the following figures:

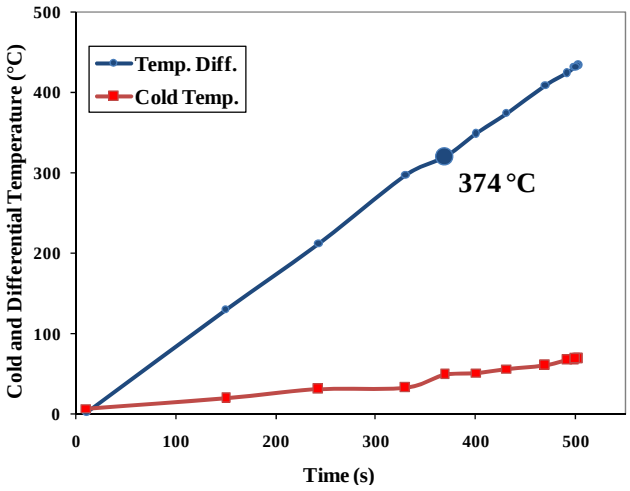

Figure 16: Temperature profile for steel wool.

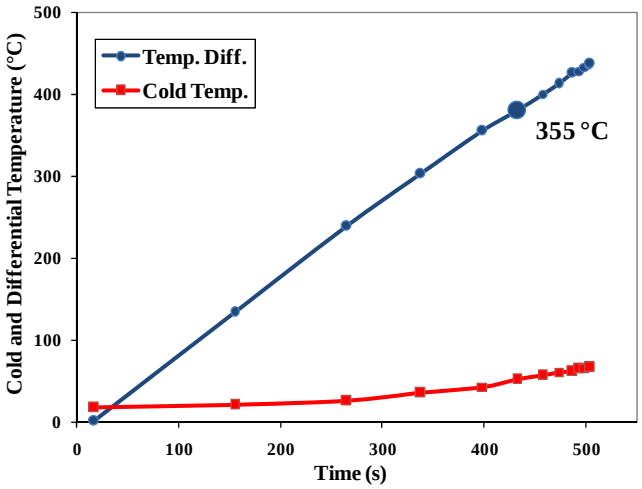

Figure 17: Temperature profile for RVC 100 PPI.

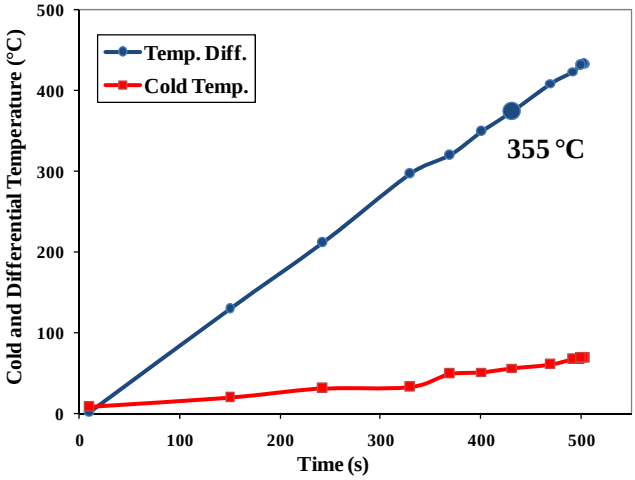

Figure 18: Temperature profile for RVC 80 PPI.

The sound pressure level in all three cases reached a maximum of approximately 103 dB. In figure 19 the results for 5.8 cm engine with three different stack materials are shown. In this case the temperature difference was recorded over 180 s time period. We can see that the RVC PPI 100 and PPI 80 have very similar results. Both materials require approximately 60 seconds and a temperature difference across the stack at about 350 °C in order to produce sound. In the case of steel wool the sound was produced after about 90 seconds and a temperature difference of about 380 °C was required for the engine to respond.

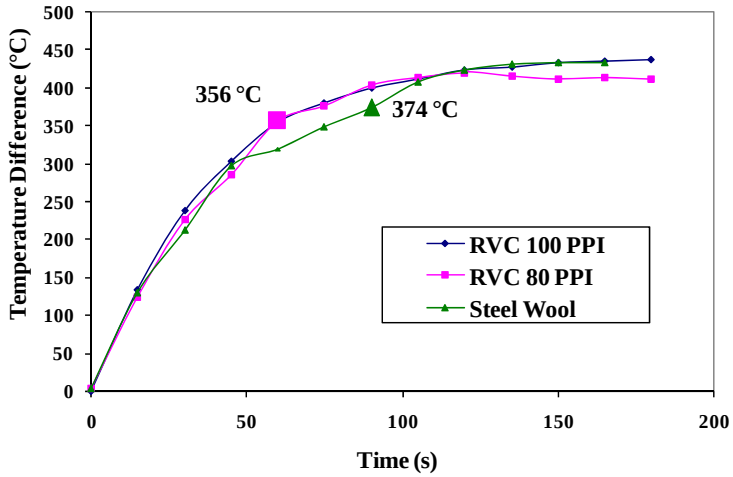

Figure 19: Temperature difference for RVC 100 PPI, 80 PPI, and steel-wool for 5.8 cm engine.

The following results represent the temperature difference and the pressure distribution for RVC 100 PPI stack in the 5.8 cm and 9.3 cm engine. In figures 20 and 21, the temperature difference across the stack and acoustic pressure distribution were plotted over 180 second time period in order to see how long it takes for the engines to produce sound and reach equilibrium. The results show that for the 5.8 cm engine we require about 60 seconds in order to produce sound, but for the 9.3 cm engine, after only 45 second, sound was produced. Also, a lower temperature difference across the stack was required for the longer engine to perform. The experimental results were compared to the

theoretical analysis from section 2.1.1. The stack used in our system was an RVC with non-uniform geometry, therefore the surface area needed to be recalculated. The RVC of 100 PPI and 80 PPI have 97% porosity. In order to calculate the surface area of the RVC it was assumed that the stack is a solid material with uniform holes across it. This assumption neglects the empty spaces between the holes and uses the porosity of the RVC to determine the approximated perimeter. Making these assumptions the surface area determined to be as follows:

$$S = \Pi \Delta x_s = \frac{1.8\pi \Delta x_s R^2}{r}. \tag{64}$$

where R is the inner radius of the stack holder, r is the radius of the small cylinders, and Δx_s is the length of the stack.

Using the new surface area formula for the 5.8 cm engine, the required temperature difference calculated is about 212 °C; and for the 9.3 cm it is about 173 °C. However, the theoretical calculations contain idealized assumptions because of irregularities in the stack geometry and the assumptions made to calculate the surface area. Also, the theoretical results do not take into account the heat loss to the environment and assume perfect conditions; therefore the theoretical results are significantly lower than the measured values.

The pressure was calculated for different temperatures to compare with the acoustic pressure measured 30 cm away from the open end. In order to calculate the acoustic pressure we assume that the open end of the engine is a point source located in the center of a sphere with a radius of 30 cm (the distance between the engine and the microphone). We calculate the radiated energy from the point source to the sphere using equation (24) from section 2.1.1. Since energy is conserved the radiated energy from

point source to the sphere must equal the radiated energy from the sphere to the surrounding environment. The equation used to determine the radiated energy from the sphere to the environment is as follows:

$$\dot{E}_{surr} = \frac{4\pi m^2 P_m^2}{\rho a}. \tag{65}$$

where m is the radius of the sphere, P_m is the RMS pressure measured, ρ is the density of air, and a is the speed of sound in air.

Setting equations (24) and (65) equal we can solve for P_m which is determined to be as follows:

$$P_m = \frac{\pi R^2 P_A}{8\sqrt{2}\, L m}. \tag{66}$$

The pressure P_m was determined to be approximately 2.3 Pa for the 5.8 cm engine and 1.8 Pa for the 9.3 cm engine for ΔT_{ext} at about 220°C.

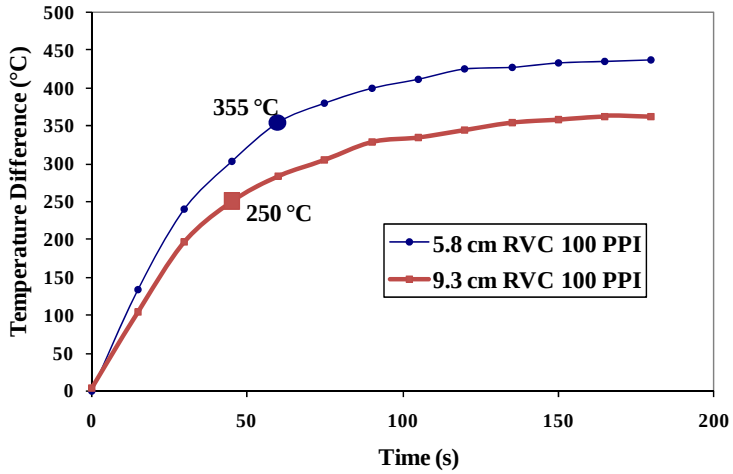

Figure 20: Temperature profile for 5.8 cm and 9.3 cm engine with RVC 100 PPI.

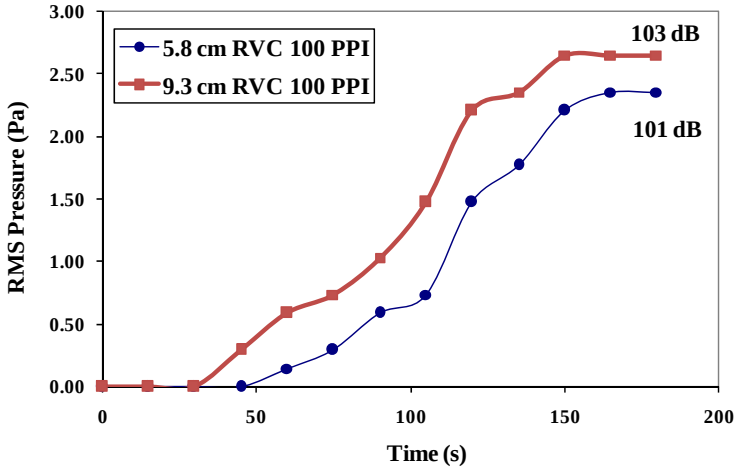

Figure 21: Acoustic pressure profile for 5.8 cm and 9.3 cm engine with RVC 100 PPI.

In order to find the average acoustic pressure amplitude the microphone was moved around the engine 180° and the effects were recorded for the RVC 100 PPI and 5.8 cm engine. In table 3 the results are tabulated.

Angle (°)	RMS Pressure (Pa)	SPL Using Microphone (dB)	SPL Using Souldlevel Meter (dB)
0	2.65	102.4	103.1
30	3.09	103.8	106.4
60	1.47	97.3	102.4
90	0.74	91.3	110.5
120	1.18	95.4	107.1
180	0.74	91.3	104.6

Table 3: Tabulated results of the acoustic pressure for RVC 100 PPI.

The same measurements were taken for the RVC 80 PPI and steel wool. The results are tabulated in table 4 and 5.

Angle (°)	RMS Pressure (Pa)	SPL Using Microphone (dB)	SPL Using Souldlevel Meter (dB)
0	2.55	102.1	102.9
30	2.95	103.4	105.9
60	1.52	97.6	101.3
90	0.95	93.5	108.2
120	1.05	94.4	107.3
180	0.65	90.2	103.5

Table 4: Tabulated results of the acoustic pressure for RVC 80 PPI.

Angle (°)	RMS Pressure (Pa)	SPL Using Microphone (dB)	SPL Using Souldlevel Meter (dB)
0	2.06	100.27	104.1
30	2.36	101.43	105.2
60	1.33	96.43	101.2
90	0.59	89.39	109.6
120	1.03	94.25	108.2
180	0.59	89.39	105.6

Table 5: Tabulated results of the acoustic pressure for steel-wool.

These results show that the strongest signal for all three cases takes place at an angle of about 30°. The SPL measured at different angles using the sound-level meter were much larger than the SPL measured using the microphone. The reason for that could be the fact that the sound-level meter is not very sensitive and captures all the noise from surroundings. The repeatability errors of these measurements were also calculated by repeating the measurements taken at each angle multiple times. The results are tabulated in table 6 and shown in figure 22. The total instrumental uncertainty is about 12% for the microphone.

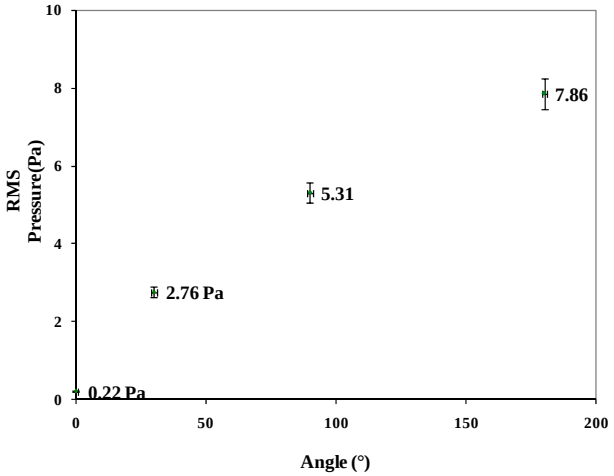

Figure 22: Acoustic pressure error measurements at different angles for 5.8 cm engine.

Angle (°)	0	30	90	180
P_1 (Pa)	0.2	2.8	5.4	8
P_2 (Pa)	0.1	2.8	5.5	8.2
P_3 (Pa)	0.3	2.8	5.3	7.8
P_4 (Pa)	0.3	2.65	5	7.35
P_5 (Pa)	0.3	2.8	5.3	7.8
P_6 (Pa)	0.2	2.65	5.1	7.55
P_7 (Pa)	0.1	2.8	5.5	8.2
P_8 (Pa)	0.2	2.8	5.4	8
Avg. Acoustic Pressure (Pa)	0.21	2.76	5.31	7.86
Oscilloscope Readability error (Pa)	0.09	0.09	0.09	0.09
Microphone Sensitivity (Pa)	0.02	0.23	0.44	0.66
Standard Dev. (Pa)	0.22	0.18	0.48	0.80
Standard Dev. of Mean (Pa)	0.07	0.06	0.15	0.25
Total Bias (Pa)	0.09	0.25	0.45	0.66
Total Uncertainty (Pa)	0.17	0.27	0.54	0.83

Table 6: Pressure uncertainty calculations for 5.3 cm engine at different angles.

Even though the results are very close for all three stack materials, we can conclude that for 5.8 cm engine the RVC 100 PPI was the most suitable stack, resulting to the highest acoustic pressure amplitude at all angles. Using this assumption and equation (65) the acoustic power $\dot{W}$ can be determined, which was 0.01 W and 0.04 W for the 5.8 cm and 9.3 cm engine respectively. Because of the uncertainties in the pressure and dimension measurement errors the uncertainties of the calculated acoustic

power for these particular configurations were about 14%. The acoustic pressure measurements were obtained by averaging the pressure amplitude obtained for the same engine conditions but different microphone positions.

The rate of heat supplied to the stack $\dot{Q}_{in}$ can be determined using equation (40). The results were about 1 W and 1.4 W for 5.8 cm and 9.3 cm engine respectively; therefore the thermoacoustic efficiency of the system can be calculated using the thermoacoustic efficiency formula as follows:

$$\eta = \frac{\dot{W}}{\dot{Q}_{in}}. \tag{67}$$

Using equation (67) the efficiency of the thermoacoustic heat engine for 5.8 cm engine is about 1% and for the 9.3 cm engine is determined to be about 2.1%. The results for both engine lengths are tabulated in table 7.

Resonator length, L	5.8 cm	9.3 cm
Measured parameters:		
Temperature difference across stack, ΔT	398°C	351°C
Radiated acoustic power, $\dot{E}_{rad}$	0.01 W	0.01 W
Frequency, f	1.4 kHz	1.0 kHz
Calculated parameters:		
Acoustic pressure amplitude in the engine, P_A	2.0 kPa	3.9 kPa
Acoustic power generated in the stack, $\dot{W}$	0.01 W	0.04 W
Rate of heat supply to the stack, $\dot{Q}_{in}$	1.00 W	1.40 W
Thermoacoustic efficiency, $\eta = \dot{W} / \dot{Q}_{in}$	1.0%	2.1%

Table 7: Tabulated experimental and theoretical results for both 5.8 and 9.3 cm engines.

3.2. Cooling Demonstrator

The main objective was to find the best stack location for each configuration and measure the absolute value of the temperatures on both ends of the stack. The following results are put together using different materials for the stack.

3.2.1. *Closed-End System*

In order to analyze the cooling demonstrator, the acoustic pressure inside the tube and the frequency of the signal were varied, and for each case the temperature difference across the stack was measured.

The closed system results show the system produces the highest temperature difference across the stack as we move the stack closer to the closed end. It was also observed that the sack side closer to the closed end of the tube was higher than the opposite end of the stack. This conclusion was made by keeping the frequency and the pressure amplitude of the signal the same during the operation, and moving the stack along the resonator. The figures below show the development of temperature difference as we move the stack in the resonator. In this case, ceramic with smaller holes were used. The frequency of the signal input was also changed in order to find the optimum frequency at which the system gives the best results. From previous experiments, it was found that the optimum frequency was in vicinity of 220 Hz; the main frequency of 218 Hz was selected. In order to analyze the system for higher and lower frequencies, the system was tested for frequencies both 100 Hz over and below the desired frequency.

This range was used because small changes in signal frequency did not change the results significantly.

In figure 23, the temperature difference dependence of frequency is shown for the stack at 13 cm. The stack was placed at 13 cm from the tube hole in the plate, the frequency of the input signal was varied, and the temperature difference was recorded in order to specify the best operating frequency for this system. These results conclude that the optimum frequency in which the system operation is most efficient is between 200 and 230 Hz. Several frequencies between 200 and 230 Hz were tested. The speaker can be used at 218 Hz over extended period of time without any damage.

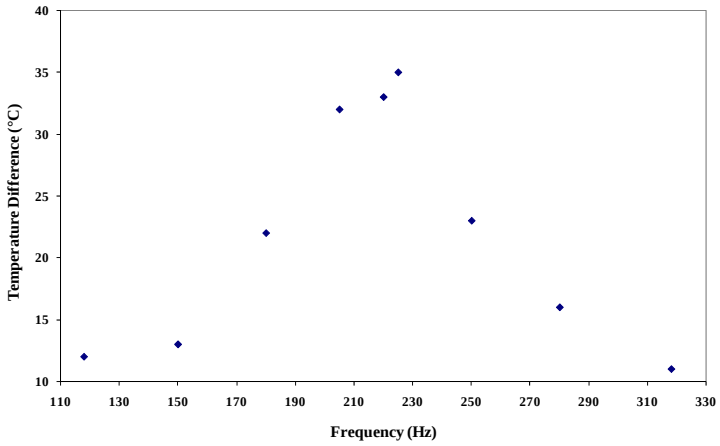

Figure 23: Frequency profile for stack at 13 cm.

Figures 24-27 show when the system operates at 218Hz, the temperature difference is the highest for each case. Furthermore, it becomes obvious that at 13 cm away from source and closer to the closed end of the resonator, the temperature difference is the largest at largest pressure amplitude and it is about 32 °C.

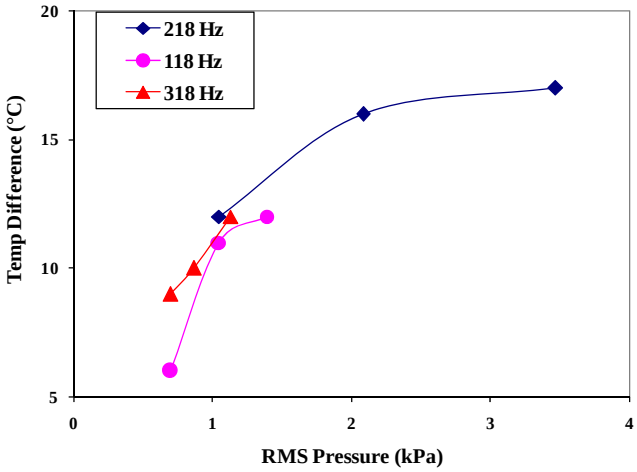

Figure 24: Temperature difference for stack located at 7 cm.

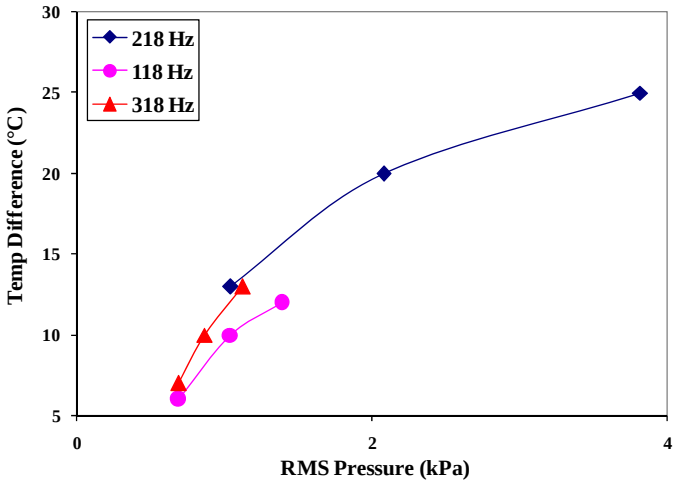

Figure 25: Temperature difference for stack located at 9 cm.

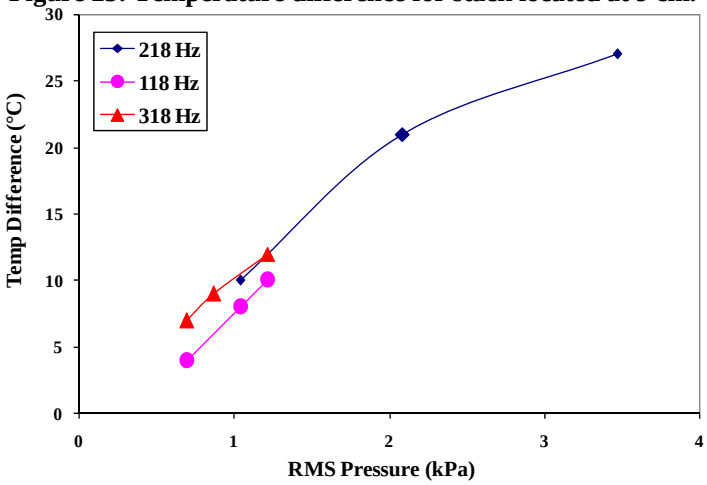

Figure 26: Temperature difference for stack located at 11 cm.

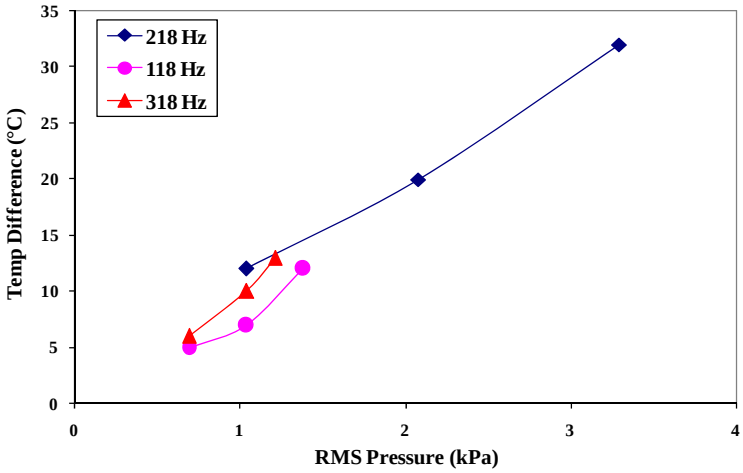

Figure 27: Temperature difference for stack located at 13 cm.

In the following figure the stack position was changed and the RMS pressure inside the tube was kept at approximately 3.5 kPa. The frequency of the input signal was changes and the temperature difference a cross the stack was recorded. In figure 28 the results for this configuration is shown.

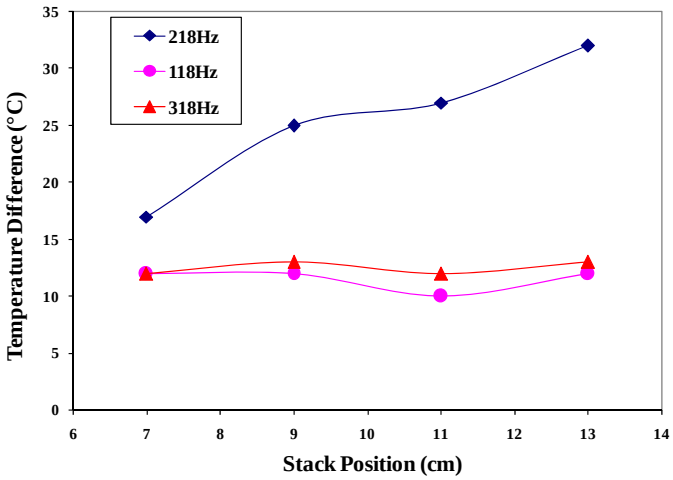

Figure 28: Temperature difference for different stack position at 3.5 kPa of RMS pressure.

Looking at these results we can again conclude that for the closed system the input signal has to be at 218Hz and the stack needs to be closed to the closed end of the resonator in order to get maximum temperature difference across the stack. For frequencies significantly above and below 218Hz the system will not be at its maximum

operating point. In figure 29 the RMS pressure is plotted against temperature difference across the stack. In this experiment the frequency was kept at 218 Hz and the position of the stack was modified to emphasize on the results previously discussed. We also can observe that with the stack located at 13 cm, the refrigeration effect is better only at highest RMS pressure. For lower RMS pressures other positions of the stack are more suitable.

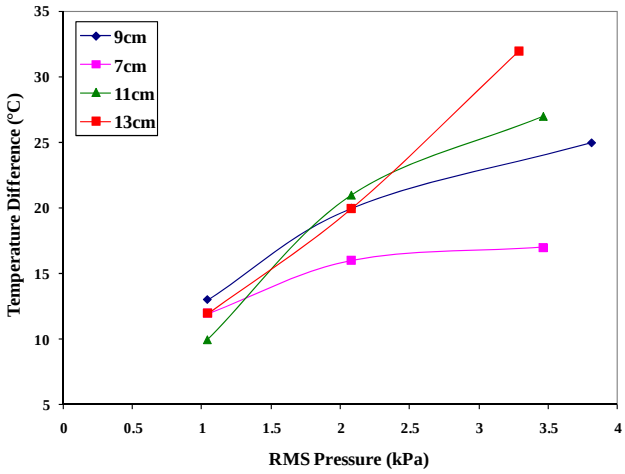

Figure 29: Temperature difference for different stack position at 218Hz.

In order to check that the repeatability error is considerably low and that these results would be the same regardless the number of times the same sets of data were taken, for each configuration, the data was taken ten times, making sure that the system starts from the same initial conditions and reaches equilibrium. In figure 30, the stack was placed at different positions, the RMS pressure inside the resonator at 3.5 kPa, and the frequency of the input signal at 218 Hz. For this setting the temperature difference was recorded 10 times and the repeatability error was calculated. The average temperature is shown for each set of data taken.

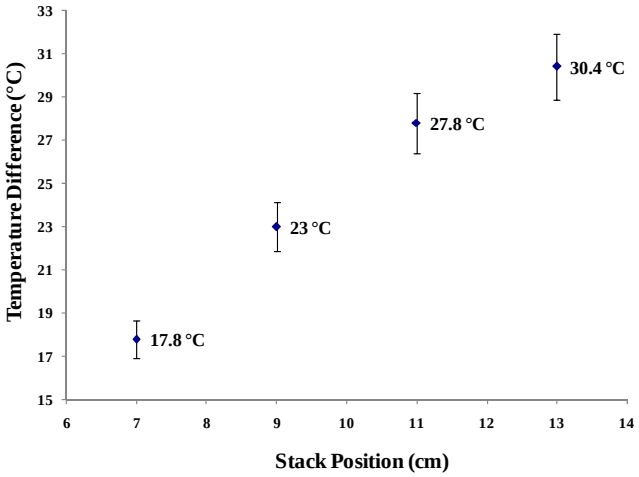

Figure 30: Repeatability error for 218 Hz signal and 3.5 kPa of RMS Pressure.

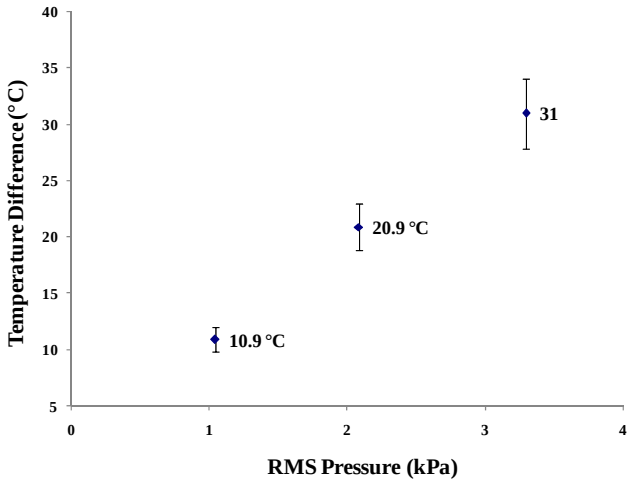

Figure 31: Repeatability error for 218 Hz signal and stack at 13 cm.

In table 6 and 7 the approach of calculating the total uncertainties are presented.

RMS Pressure (kPa)	3.29	2.08	1.04
T_1 (°C)	32	20	12
T_2 (°C)	31	21	11
T_3 (°C)	32	20	10
T_4 (°C)	32	22	12
T_5 (°C)	30	21	11
T_6 (°C)	30	22	10
T_7 (°C)	30	20	11
T_8 (°C)	31	22	11
T_9 (°C)	32	20	10
T_{10} (°C)	30	21	11
Avg. Temp. (°C)	31.00	20.90	10.90
Thermocouple Linearity (°C)	0.7	0.7	0.7
Thermocouple Sensitivity (°C)	0.35	0.35	0.35
Thermometer Sensitivity (°C)	1.09	1.06	1.03
Zero Shift (°C)	0.5	0.5	0.5
Standard Dev. (°C)	0.94	0.88	0.74
Standard Dev. of Mean (°C)	0.30	0.28	0.23
Total Bias (°C)	1.43	1.41	1.39
Total Uncertainty (°C)	2.88	2.84	2.79

Table 8: Uncertainty calculation for different RMS pressures.

Stack Position (cm)	7	9	11	13
T_1 (°C)	32	27	25	17
T_2 (°C)	31	27	23	17
T_3 (°C)	30	28	22	18
T_4 (°C)	30	29	23	18
T_5 (°C)	29	27	21	19
T_6 (°C)	29	27	23	17
T_7 (°C)	31	28	22	18
T_8 (°C)	32	27	25	17
T_9 (°C)	30	29	23	18
T_{10} (°C)	30	29	23	19
Avg. Temp. (°C)	30.40	27.80	23.00	17.80
Thermocouple Linearity (°C)	0.7	0.7	0.7	0.7
Thermocouple Sensitivity (°C)	0.35	0.35	0.35	0.35
Thermometer Sensitivity (°C)	1.09	1.08	1.07	1.05
Zero Shift (°C)	0.5	0.5	0.5	0.5
Standard Dev. (°C)	1.07	0.92	1.25	0.79
Standard Dev. of Mean (°C)	0.34	0.29	0.39	0.25
Total Bias (°C)	1.43	1.43	1.42	1.40
Total Uncertainty (°C)	1.59	1.54	1.62	1.49

Table 9: Uncertainty calculation for different stack positions.

Finally, for the best conditions that were established in previous steps, different stack materials were tested in order to establish the most efficient stack material for the system. In figure 32 the final results are shown.

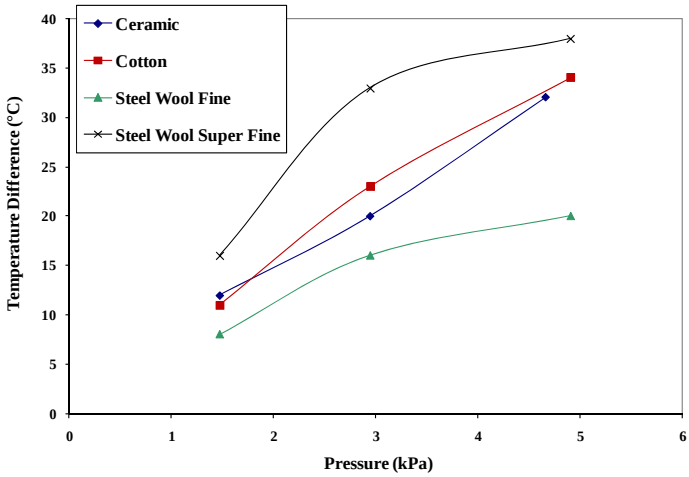

Figure 32: Temperature difference for different stack material at 13 cm.

The results show that for this configuration the super-fine steel wool is the best material for the stack resulting to a maximum temperature difference of 38 °C across the stack.

In order to study the system from start to the time the system reaches equilibrium, the change in temperature was recorded over time. Using this method, we can see the changes in temperature of both sides of the stack and see how long it takes for the system to reach equilibrium. In figure 33, the temperature difference is recorded in 15 second time steps. Since it does not take a long time to reach equilibrium, the first portion of the test was repeated at a 5 second time steps. These results are shown in figure 34.

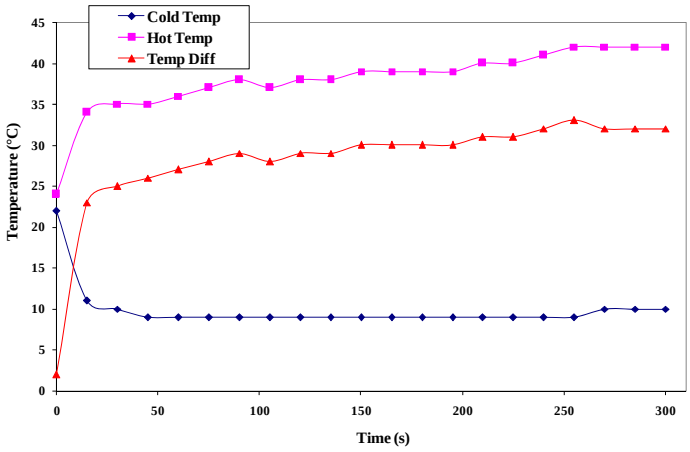

Figure 33: Temperature profile recorded every 15 seconds.

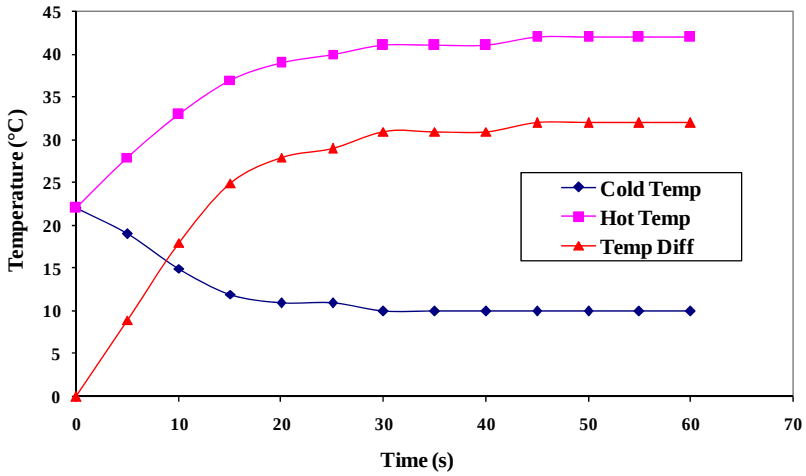

Figure 34: Temperature profile recorded every 5 seconds.

Based on these results, we conclude that the refrigerator is able to reach equilibrium and maximum temperature difference relatively quickly. We also see the trend of the cold side and the hot side of the stack. The temperatures are the same at the initial point in the system, but the temperature of the cold end drops and after about 30 seconds remains constant; the temperature of the hot end on the other hand increases and after about 30 seconds stays constant. In the case of the closed end refrigerator, the stack side that is away from the source and close to the closed tube end is hot, and the stack side close to the source is cold. These trends are sensitive to the input signal frequency and acoustic pressure amplitude. Any change in these values will rather amplify or reduce the temperature difference across the stack. These results can be compared with theory using methodology described in section 2.1.2. The enthalpy flow and the pressure distribution across the tube can be calculated. In figure 35, we can see the enthalpy flow has positive values and it increases as we move along the tube. These results suggest that the temperature of the stack side facing the closed end should be larger than the temperature of the stack side facing the source. The following calculations were made for a tube with a total length of 29 cm at frequencies of 118, 218, 318, and 418 Hz.

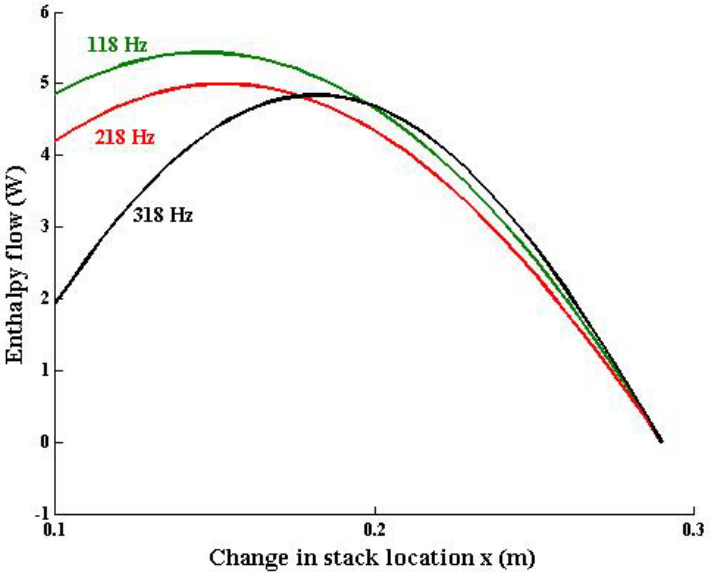

Figure 35: Enthalpy flow across the tube for a close-ended system.

3.2.2. Open System

The same approach was taken for the open-end system as for the closed-end system. In the case of the open system, the stack needs to be closer to the sound source for better performance. At this point, all the experiments are done using the steel wool as the stack material, since the steel wool found to be the best choice for these configurations. The temperature difference across the stack is much lower in the case of open-end and the measured temperature close to the source is lower than the temperature of the stack side close to the open end. Therefore the temperature difference across the stack will be defined by subtracting the top temperature from the bottom temperature. The following figures show the results for different stack position and different frequencies. Because of the pressure transducer location, in open-end configuration, the displacement range of the stack is small.

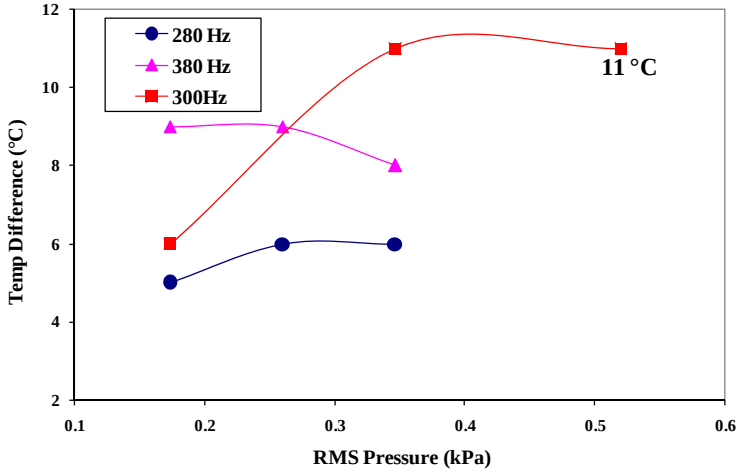

Figure 36: Temperature difference for stack located at 6 cm.

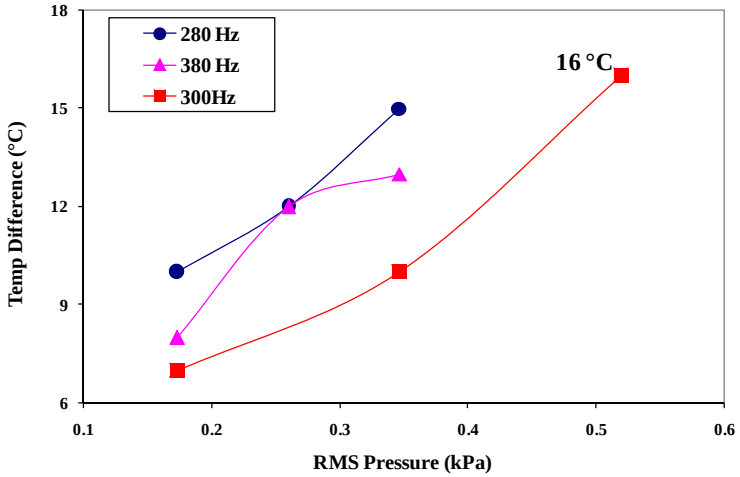

Figure 37: Temperature difference for stack located at 7 cm.

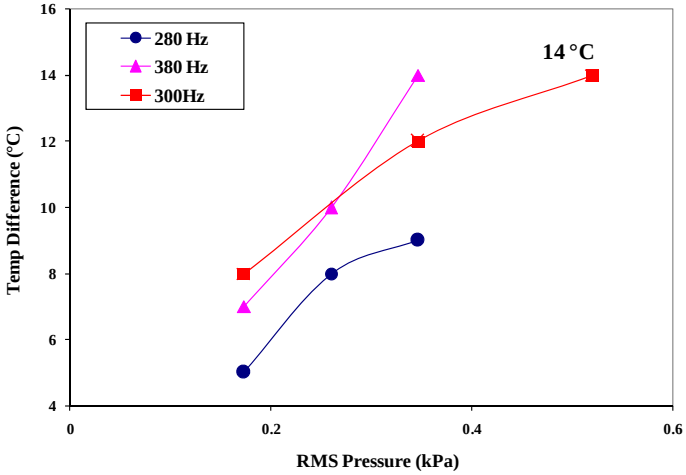

Figure38: Temperature difference for stack located at 8 cm.

In figure 40 the frequency profile is shown for the stack at 6 cm. The stack was placed at 6 cm and the frequency of the input signal was varied; and the temperature difference across the stack was recorded in order to specify the best operating frequency for this configuration. From these results we can conclude that the optimum frequency in which the system operates most efficiently is around 350 Hz.

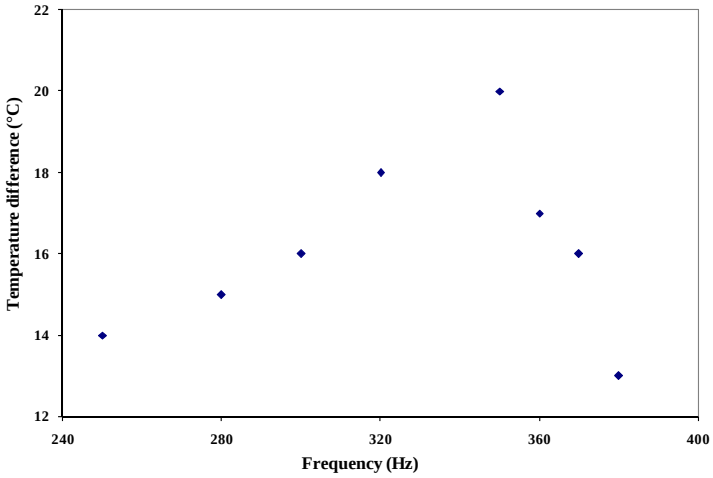

Figure 39: Frequency profile for stack at 6 cm.

Looking at results from figures 36-39, we can conclude that the stack has to be close to the source for an open-ended system in order to achieve the highest temperature difference across the stack. In this case, at 6 cm away from the source the temperature difference across the stack reached 16 °C. In figure 41 the theoretical enthalpy flow estimation for an open-ended demonstrator is shown. From the results obtained, we can see that the enthalpy flow is negative, meaning that the temperature of the stack side close to the open-end must be lower than the temperature of the stack side close to the source. In this case, the theoretical results confirm the experimental data. These calculations were conducted following the steps that were analyzed in section 2.2.1. The calculations were computed for a tube with a total length of 17.5 cm and for the output frequencies of 250, 300, 350, and 400 Hz.

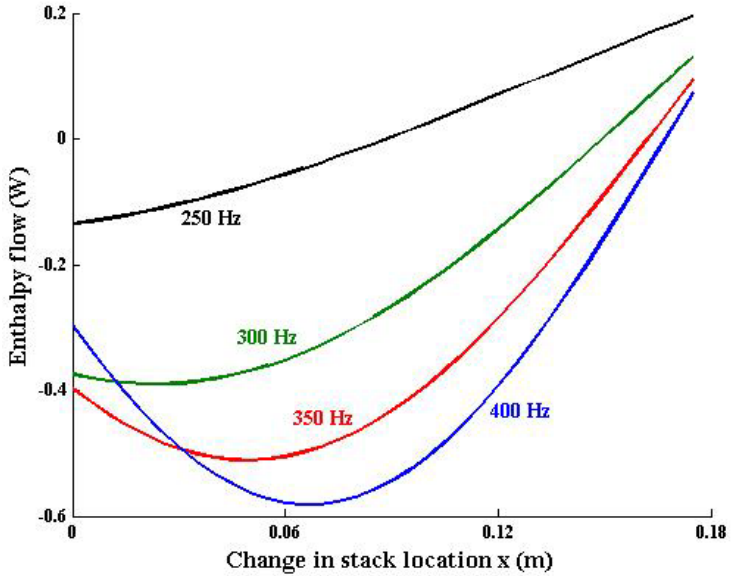

Figure 40: Enthalpy flow across the tube for an open-ended system.

The next step follows the same procedure as the closed-end system. The acoustic pressure amplitude inside the resonator was kept the same, while the stack position was varied. Knowing that the optimum operating frequency is about 350 Hz, the frequency was kept at 330 Hz and the stack position was changed. These measurements were taken to verify the best operation frequency and the best stack position. In figure 42 and 43 these results are plotted.

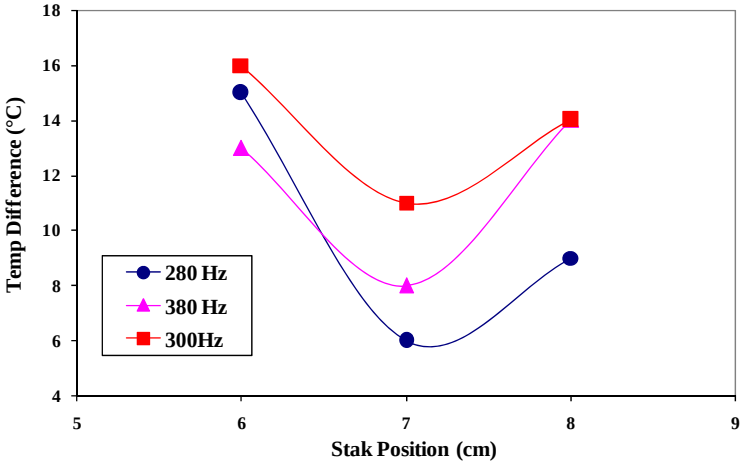

Figure 41: Temperature difference for different stack position at 0.35 kPa of RMS pressure.

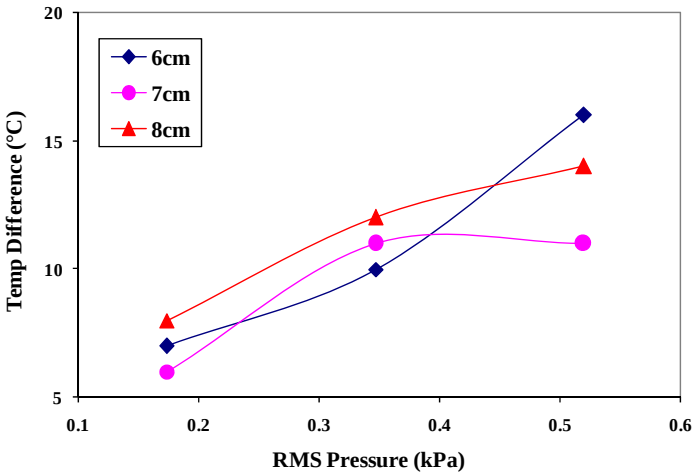

Figure 42: Temperature difference for different stack position at 330Hz.

The repeatability error was checked by following the same procedure as the closed-end system. The results are tabulated and graphed in the following tables and figures.

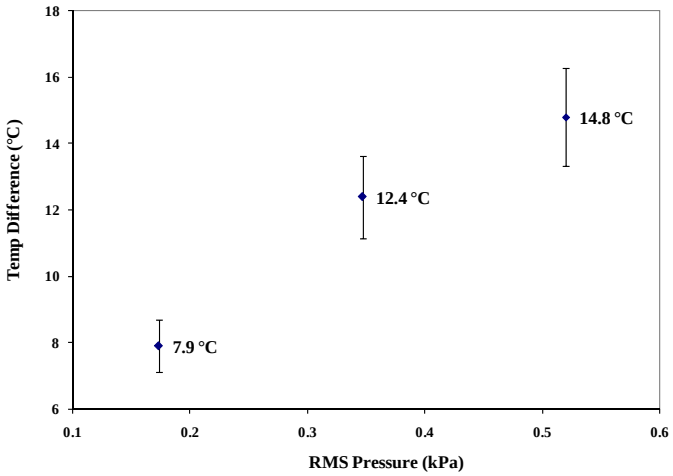

Figure 43: Repeatability error for 330 Hz signal and 0.5 kPa of RMS pressure.

Stack Position (cm)	6	7	8
T_1 (°C)	14	10	11
T_2 (°C)	15	10	11
T_3 (°C)	15	11	12
T_4 (°C)	16	11	12
T_5 (°C)	16	11	13
T_6 (°C)	16	11	13
T_7 (°C)	17	12	13
T_8 (°C)	15	11	12
T_9 (°C)	15	11	12
T_{10} (°C)	16	11	13
Avg. Temp. (°C)	15.50	10.90	12.20
Thermocouple Linearity (°C)	0.7	0.7	0.7
Thermocouple Sensitivity (°C)	0.35	0.35	0.35
Thermometer Sensitivity (°C)	1.05	1.03	1.04
Zero Shift (°C)	0.5	0.5	0.5
Standard Dev. (°C)	0.85	0.57	0.79
Standard Dev. of Mean (°C)	0.27	0.18	0.25
Total Bias (°C)	1.40	1.39	1.39
Total Uncertainty (°C)	1.50	1.43	1.48

Table 10: Uncertainty calculation for different stack positions.

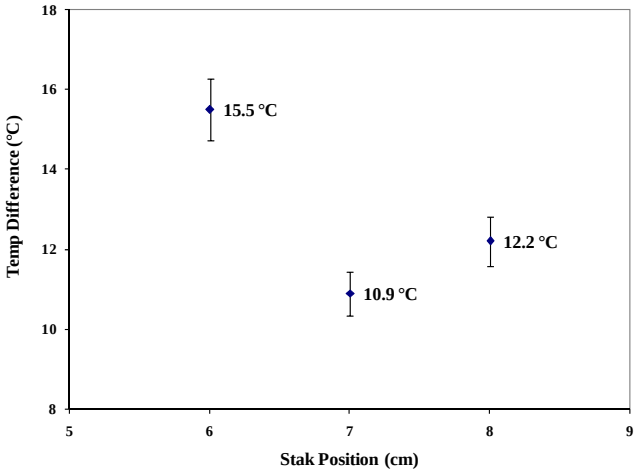

Figure 44: Repeatability error for 330 Hz signal and stack at 6 cm.

RMS Pressure (kPa)	0.52	0.35	0.17
T_1 (°C)	16	12	8
T_2 (°C)	15	12	8
T_3 (°C)	16	13	9
T_4 (°C)	13	13	7
T_5 (°C)	14	13	8
T_6 (°C)	14	12	7
T_7 (°C)	16	13	9
T_8 (°C)	15	12	8
T_9 (°C)	13	13	7
T_{10} (°C)	16	11	8
Avg. Temp. (°C)	14.80	12.40	7.90
Thermocouple Linearity (°C)	0.7	0.7	0.7
Thermocouple Sensitivity (°C)	0.35	0.35	0.35
Thermometer Sensitivity (°C)	1.04	1.04	1.02
Zero Shift (°C)	0.5	0.5	0.5
Standard Dev. (°C)	1.23	0.70	0.74
Standard Dev. of Mean (°C)	0.39	0.22	0.23
Total Bias (°C)	1.40	1.39	1.38
Total Uncertainty (°C)	1.60	1.46	1.46

Table 11: Uncertainty calculation for different RMS pressures.

The repeatability error is marginal in the case of open-end system as well; therefore the experimental results are accurate. After finding the most suitable conditions (such as the best operation frequency, acoustic pressure amplitude, and stack position) the system was tested for different stack materials. In figure 46 the results for different stack materials are shown.

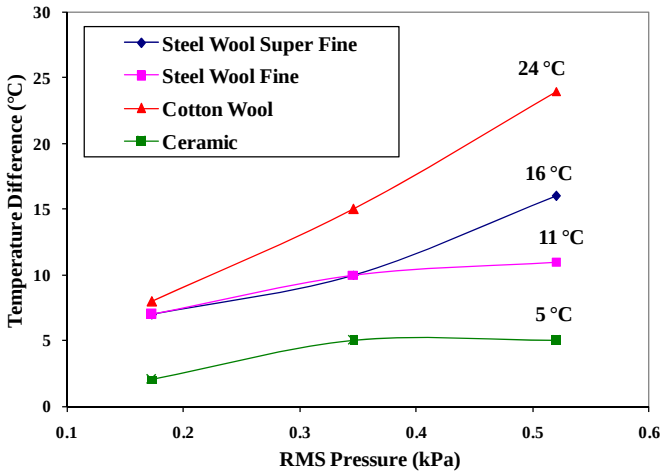

Figure 45: Temperature difference for different stack materials at 6 cm.

Under these conditions, the cotton wool reached the highest temperature difference. However cotton wool was unstable and was difficult to keep in the same position for extended amount of time. It was also difficult to change the acoustic pressure amplitude. In addition, the results show that in the case of the open-ended system, a steel wool is the best option for the stack material.

Chapter 4

Conclusion and Recommendations

4. Conclusions and Recommendations

In this study a thermoacoustic heat engine was successfully built and tested for different conditions. During the tests, different stack materials and engine lengths were used. The temperature difference across the stack and the acoustic pressure amplitude were measured and compared with theoretical values.

The acoustic power radiated by the 5.8 cm long engine, with 100 PPI RVC as the stack, is about 0.01 W, with a sound pressure level of approximately 106 dB measured 30 cm away from the open end of the engine. There are many variables that contribute to exergy loss and performance reduction in the system. One possible way to increase the performance of the heat engine will be to minimize the heat losses to the surrounding medium. An important factor in the engine construction is the sealing between its parts. The engine did not produce any sound before the gaskets were introduced between the flanges of the system components. Presently, a flame is applied as a heat source in our system; in the future the flame can be replaced with other more efficient heat sources. By implementing a piezoelectric pressure transducer at the open end of the engine, the acoustic power can be converted to electric power. Hence, the thermoacoustic heat engine can be used as a small scale power source.

The microphone was placed outside the engine to measure the pressure amplitude in the external acoustic field. In order to eliminate acoustic reflection uncertainty, the system can be placed in an anechoic chamber that would minimize these reflections. The acoustic power inside the engine is of main importance; therefore, a small cavity can be added to the engine structure, where a pressure transducer can be inserted. In the future,

temperature and pressure data can be taken using a data acquisition system for better time resolved measurements.

A cooling demonstrator was also built in this study. It was tested in different conditions, open- and closed-end configurations. The results gave us an idea about the most favorable stack material and location in each system. In both open and closed-end systems, super fine steel wool was determined to be the best material used for stack.

In the closed system the stack has to be close to the closed end away from the source to produce higher temperature difference across the stack. The temperature of the stack side close to the cap was higher than the temperature of the stack side closer to the source. In the case of the open system the effects were reversed; the closer the stack was to the source and away from the open end, the higher the temperature difference across the stack was observed. We can see that by changing the tube boundary conditions the cooling effect can be influenced. It can be recommended to test other materials for the stack, which can result in higher temperature differences across the stack. Since the temperatures were taken using thermocouples connected to thermometers, recording the change of temperature over time at a fast rate was difficult. The temperatures can be recorded using a data acquisition system for better time resolution. The pressure amplitude inside the resonator was monitored by a pressure transducer that was connected to an oscilloscope. In the future, this pressure transducer can be also connected to a data acquisition system for automatic readings. In order to use the full range of our amplifier and maximize the heat pumping in the cooling demonstrator, more powerful speakers can be implemented in the system.

References

[1] G.W. Swift: Thermoacoustic Engines, Journal of Acoustic Society of America, 84:1145, July 1988.

[2] G.W. Swift: What is thermoacoustics?, Journal of Acoustic Society of America, 1-3, April 2004.

[3] C. Sondhauss: Ueber dei Schallschwingungen der Luft in erhitzten Glasrhren und in gedeckten Pfeifen von ungleicher Weite. Annalen der Physik und Chemie, 79:1-34, 1850.

[4] K. T. Feldman: Review of the literature on Sondhauss thermoacoustic phenomena, Journal of Sound and Vibration, 7:71-82, 1968.

[5] K. T. Feldman: Review of the literature on Rijke thermoacoustic phenomena. Journal of Sound and Vibration, 7:3-89, 1968.

[6] Lord Rayleigh: The explanation of certain acoustical phenomena, 18:319-321, 1878, 2004

[7] O. Lucas, K. Meeuwissen: Design and Construction of a Thermoacoustic Device, Journal of Acoustic Society of America, September 2001.

[8] T. J. Hofler, J. A. Adeff: An optimized miniature Hofler tube, American Journal of Physics, 1529-7853, October 2006.

[9] A. G. Chakhovskoi, C. E. Hunt, G. Forsberg, T. Nilsson, P. Persson: Reticulated vitreous carbon field emission cathodes for light source application, Vacuum Microelectronics Conference, 263-4, July 2001.

[10] D. Sun, L. Qiu, W. Zhang, W. Yan, G. Chen: Energy Conversion and Management: Investigation on traveling wave thermoacoustic heat engine with high pressure amplitude, 46:281-291, February 2005.

[11] N. Rott. Thermoacoustics. Advanced Applied Mechanics, 20:35-175, 1980.

[12] N. Rott. Thermally driven acoustic oscillations, part III: Second-order heat flux. Z. Angew. Math Physics forum, 26:43-49, 1975.

[13] S. Backhaus, E. Tward, M. Petach: Thermoacoustic Power Systems for Space Applications, Space Technology and Applications International Forum, 939-944, 2002.

[14] S. Backhaus, E. Tward, M. Petach: Traveling-wave thermoacoustic electric generator, Applied Physics Letters, 85:1085. August 2004.

[15] P. Schewe, B. Stein: Acoustically Powered Deep-Space Electric Generator, <www.aip.org/pnu/2004/split/695-2.html>.

[16] S. Backhaus, G. Swift: A thermoacoustic-Stirling heat engine: Detailed Study, Journal of Acoustical Society of America, Vol. 107, 3148-3166, 2000.

[16] "STAR Motors/Alternators - 1S102M/A." Qdrive resonant power systems. 2006. <http://www.qdrive.com/index.php?id=63>.

[17] O. G. Symko, E. Abdel-Rahman, Y. S. Kwon, M. Emmi, R. Behunin: Design and development of high-frequency thermoacoustic engines for thermal management in microelectronics. Microelectronics Journal, 35:185-191. September 2003.

[18] K. Matveev, A. Wekin, C. Richards, N. Shafiei-Tehrany: Coupling between standing-wave thermoacoustic engine and piezeoelectric transducer. ASME International Mechanical Engineering and Exposition. November 2007. Seattle, Washington.

[19] N. Shafiei-Tehrany, C. Shung Lin, J. Ahn, K. Matveev: Development of combustion-driven small thermoacoustic engine. Spring Meeting of the Western States Section of the Combustion Institute. March 2008. Los Angeles, California.

[20] Corning Environmental Technologies. 2008. <http://www.corning.com/environmentaltechnologies/products-applications/ceramic-substrates/>.